Lithos 323 (2018) 218–237

Contents lists available at ScienceDirect

Lithos

journal homepage: www.elsevier.com/locate/lithos

Evidence of polygenetic carbon trapping in the Oman Ophiolite: Petro-structural, geochemical, and carbon and oxygen isotope study of the Wadi Dima harzburgite-hosted carbonates (Wadi Tayin massif, Sultanate of Oman)

J. Noël [a,*], M. Godard [a], E. Oliot [a], I. Martinez [b], M. Williams [c], F. Boudier [a], O. Rodriguez [d], C. Chaduteau [b], S. Escario [a], P. Gouze [a]

[a] Géosciences Montpellier, CNRS, University of Montpellier, Montpellier 34095, France
[b] IPGP, Université Paris Diderot, Paris 75005, France
[c] Research School of Earth Sciences, Australian National University, Canberra, Australia
[d] Voxaya SAS, Montpellier 34090, France

ARTICLE INFO

Article history:
Received 15 March 2018
18 June 2018
Accepted 14 August 2018
Available online 20 August 2018

Keywords:
Peridotite carbonatization
Carbonate veins
Serpentinization
Trace elements
Oman Ophiolite

ABSTRACT

The Wadi Dima area (Oman Ophiolite) exposes partially altered to highly serpentinized harzburgites that are cross-cut by intense (>20 Vol%) carbonate veining. We identified a sequence of 3 types of carbonate veins with compositions ranging from calcite to dolomite (Mg/Ca = 0-0.85). Type 1 carbonates occur as a fine diffuse vein network, locally replacing olivine cores, penetrative into the serpentinized harzburgites. They have depleted trace elements abundances (e.g., Yb < 0.2 × C1-chondrite) relative to other Wadi Dima carbonates, exhibit negative Ce and positive Y, U anomalies and a broad range in $\delta^{13}C_{V\text{-}PDB}$ (-5 to -15‰) and $\delta^{18}O_{SMOW}$ (18 to 31‰). These compositions are consistent with precipitation after seawater-derived fluids and/or fluids in equilibrium with mantle rocks and serpentines during cooling of oceanic lithosphere (110 to 15°C). Type 2 carbonates are localized in veins, which acted as main flow paths for fluids interacting with peridotites in the exhumed Oman mantle lithosphere (50°C-10°C). The orientation of these veins is controlled by the crystallographic anisotropy of Oman mantle peridotites. Type 2 carbonates record two stages. The first involved the formation of large calcite crystals of composition similar to Type 1 carbonates (trace element depleted; $\delta^{13}C_{V\text{-}PDB\ B}$ = -4 to -9‰ and $\delta^{18}O_{SMOW}$ = 26 to 30‰), which during the second stage were recrystallized to form dolomite and calcite microcrystals (trace element enriched; $\delta^{13}C_{V\text{-}PDB}$ = -7 to -13‰ and $\delta^{18}O_{SMOW}$ = 29 to 32‰), after fluids sampling different sources including contributions of sediment-derived components. They were most likely formed at shallow depths and record the transition from oceanic to continental settings during late Cretaceous ophiolite obduction. Type 3 veins reactivate Type 2 veins. They comprise dominantly calcite and dolomite microcrystals (Light REE enriched patterns) with isotopic compositions ($\delta^{13}C_{V\text{-}PDB\ B}$ ~ -7 to -8‰; $\delta^{18}O_{SMOW}$~ 28 to 32‰) consistent with precipitation at low temperatures (T°<30°C) from surface/meteoric fluids. Type 3 veining is probably triggered by ophiolite uplift during the Oligocene to early Miocene. Our study presents new insights into the role of the initial mantle anisotropy in the orientation of the vein network and of principal flow paths during serpentinization and carbonatization of mantle peridotites. It also highlights the highly variable carbon isotope composition of carbonates and suggest different origins for these heterogeneities: the carbon isotope composition of the early Type 1 carbonates dispersed in the poorly connected peridotites is locally modified by serpentinization reactions whilst the carbon isotope compositions of Type 2 and 3 carbonates record mixing of fluids from different sources in high flow veins.

1. Introduction

Carbonate mineralization in peridotites is an alteration process associated with serpentinization commonly observed from oceanic hydrothermal systems (Früh-Green et al., 2003; Kelley et al., 2001), to subduction zones (Alt et al., 2012; Deschamps et al., 2013) and

* Corresponding author.
E-mail address: Julie.Noel@gm.univ-montp2.fr (J. Noël).

https://doi.org/10.1016/j.lithos.2018.08.020
0024-4937/

ophiolites (Barnes et al., 1978; Cipolli et al., 2004; Dewandel et al., 2005; Kelemen et al., 2011; Neal and Stanger, 1985; Schwarzenbach et al., 2013, 2016). It results in the formation of carbonate vein networks, ophicarbonates and carbonate-sedimented breccia locally which are observed in the shallow mantle lithosphere along mid-oceanic ridges (Bach et al., 2011; Eickmann et al., 2009; Früh-Green et al., 2003; Schroeder et al., 2015) and in ophiolitic mantle sections (Kelemen et al., 2011; Quesnel et al., 2016; Schwarzenbach et al., 2013, 2016; Zedef et al., 2000). Carbonate mineralization reactions, hereafter referred to as carbonatization, and serpentinization affect the main constitutive minerals of the mantle lithosphere: olivine and pyroxenes. Dissolution of these mafic silicates provides the majority of magnesium and calcium for carbonates. Serpentinization and carbonatization reactions are commonly written (e.g., Kelemen et al., 2011):

$$\underset{\text{(olivine)}}{6(Mg,Fe)_2SiO_4} + 7H_2O = \underset{\text{(serpentine)}}{3(Mg,Fe)_3Si_2O_5(OH)_4} + \underset{\text{(magnetite)}}{Fe_3O_4} + H_2 \quad (R1)$$

$$\underset{\text{(orthopyroxene)}}{3(Mg,Fe)SiO_3} + 2H_2O = \underset{\text{(serpentine)}}{(Mg,Fe)_3Si_2O_5(OH)_4} + \underset{\text{(silice)}}{SiO_2(aq)} \quad (R2)$$

$$\underset{\text{(olivine)}}{4Mg_2SiO_4} + 4H_2O + 2CO_2 = \underset{\text{(serpentine)}}{2Mg_3Si_2O_5(OH)_4} + \underset{\text{(magnesite)}}{2MgCO_3} \quad (R3)$$

$$\underset{\text{(olivine)}}{4Mg_2SiO_4} + \underset{\text{(Ca-pyroxene}}{CaMgSi_2O_6} + 6H_2O + CO_2 = \underset{\text{(serpentine)}}{3Mg_3Si_2O_5(OH)_4} + \underset{\text{(calcite/aragonite)}}{CaCO_3} \quad (R4)$$

$$\underset{\text{(Fe-olivine)}}{6Fe(II)_2SiO_4} + 7H_2O = \underset{\text{(Fe-serpentine}}{3Fe(II)_3Si_2O_5(OH)_4} + \underset{\text{(magnetite)}}{Fe(III)_2Fe(II)O_4} + H_2(aq) \quad (R5)$$

The oxidation of Fe(II) of mantle minerals during serpentinization (R1 and R5) produces oxides (e.g., magnetite) and generates H_2-bearing reduced (low oxygen fugacity) fluids (e.g., Allen and Seyfried, 2003; Beard et al., 2009; Janecky and Seyfried, 1986; Klein et al., 2009). These reactions give rise to hydrogen- and methane-rich ultramafic-hosted hydrothermal vents along mid-oceanic ridges (e.g., Delacour et al., 2008; Douville et al., 2002; Früh-Green et al., 2003, 2004; Früh-Green et al., 2004; Proskurowski et al., 2008) and to high pH, hydrogen-rich peridotite-hosted alkaline springs commonly observed in ophiolites (e.g., Barnes et al., 1978; Cipolli et al., 2004 ; Dewandel et al., 2005; Neal and Stanger, 1985; Paukert et al., 2012; Schwarzenbach et al., 2016). Abiotic organic carbon components were also measured in fluids from oceanic ultramafic-hosted hydrothermal systems (Lang et al., 2018; Proskurowski et al., 2008) and ophiolite-hosted alkaline springs (D'Alessandro et al., 2018). Their formation has been ascribed to carbon reduction reactions in presence of high H_2 concentrations following a Fischer-Tropsch-type-reduction reaction (Proskurowski et al., 2008):

$$CO_{2aq} + [2 + (m/2n)]H_2 \rightarrow (1/n)CnHm + 2H_2O \quad (R6)$$

Carbonatization and carbonation reactions represent an efficient mechanism for trapping carbon into the serpentinized mantle lithosphere, which is now considered one of the principal reservoirs for carbon cycling into subduction zones, in addition to carbonate-bearing sediments and the altered oceanic crust (Kelemen and Manning, 2015).

Experimental data indicate that carbonatization can occur concurrently with serpentinization at pressure conditions typical of oceanic hydrothermalism (≤ 200 MPa) but with an offset in the temperature range for their optimal reaction kinetics, which is 250-300°C and 180-190°C for serpentinization and carbonatization respectively (see compiled dataset in Kelemen and Matter, 2008). Both serpentinization and carbonatization reactions are exothermic, and Kelemen et al. (2011) suggested that this would allow sustained reaction to occur over a broad range of temperature conditions. These conditions of reactions stabilities support the concept that carbonatization could become a method for safe and permanent carbon storage of excess atmospheric CO_2 produced through anthropogenic emissions (Kelemen and Matter, 2008; Seifritz, 1990).

The mantle section of the Oman Ophiolite shows evidence of past oceanic and active continental serpentinization and CO_2 mineralization (see review in Kelemen et al., 2011). It offers exceptional mantle exposures and, thus it is an ideal site to investigate serpentinization and associated carbon trapping processes. Recent studies of the chemistry of the peridotite-hosted alkaline springs in Oman (Chavagnac et al., 2013a, 2013b; Miller et al., 2016; Paukert et al., 2012) and of associated travertines and carbonate veins (Falk et al., 2016; Mervine et al., 2014) have shown that serpentinization and carbon trapping reactions are still active today in this ophiolite. However, the actual hydrodynamic systems, the fluid sources and their relation to carbon trapping and serpentinization reactions remain poorly documented. Also, the relative contributions of (i) oceanic hydrothermal circulation, (ii) fluid contamination during obduction and (iii) present-day weathering to the formation of peridotite-hosted carbonates is poorly known. Large uncertainties also exist concerning the tectonic, physical and chemical processes controlling carbon trapping and their coupling to serpentinization at these different stages of the hydrothermal alteration of the ophiolite mantle section. In particular, the development of flow paths in relation to serpentinization remains to be documented in the low-permeability peridotite basement (e.g., fracturing in relation to tectonic and/or inherited mantle structure; Boudier et al., 2005; reaction driven cracking; Jamtveit et al., 2009; Kelemen et al., 2011; Kelemen and Hirth, 2012; Macdonald and Fyfe, 1985; Plümper et al., 2012; Rudge et al., 2010; Zhu et al., 2016).

This study focuses on the characterization of mechanical, mineralogical and geochemical process driving serpentinization and carbon trapping in the Oman Ophiolite mantle section from oceanic to continental settings. The main goals are: (1) to identify and characterize flow paths, the composition of fluids and the timing of formation of serpentine and carbonate minerals (2) to understand the origin and mechanisms of serpentinization and carbon trapping during the different stages of the Oman Ophiolite formation, from oceanic hydrothermalism at spreading ridges to modern weathering at the ophiolite. We report detailed petro-structural and geochemical study of a series of oriented samples of carbonate veins and their serpentinized peridotite host from the Wadi Dima area (Wadi Tayin massif, Sultanate of Oman). The combination of structural, micro-textural, trace elements data and C-O isotopic compositions provide new insight regarding the development of microcracks and flow paths, the evolution of fluid-rock interaction and the timing of carbonate precipitation in the mantle section of the Oman Ophiolite.

2. Geological setting and sampling

The Oman Ophiolite is located in the eastern part of the Arabian Peninsula (Sultanate of Oman and United Arab Emirates; Fig. 1). It preserves the largest and the best-exposed segment of Tethyan oceanic lithosphere, and has been extensively studied (e.g.; Coleman, 1981; Glennie et al., 1973; Nicolas et al., 2000; Searle and Cox, 2002). We summarize here its main geological characteristics to provide a framework for our high resolution petro-structural and geochemical study. The Oman Ophiolite exposes a complete section of Penrose type layered oceanic crust (upper volcanics, sheeted dike complex and plutonic rocks) overlying mantle peridotites over an area 500 km along strike, and exhibits thicknesses of up to 15 km. The mantle peridotites preserve microstructures acquired during ridge accretion (Nicolas et al., 2000). The base of the Oman Ophiolite consists of a metamorphic sole, composed of amphibolite grade metamorphosed oceanic sediments and volcanic rocks. It overlies the allochthonous Hawasina formations, consisting of weakly metamorphosed pelagic sediments and interbedded volcanic rocks. The Hawasina nappes lay atop the Permian to Cenomanian autochthonous continental shelf carbonate deposits,

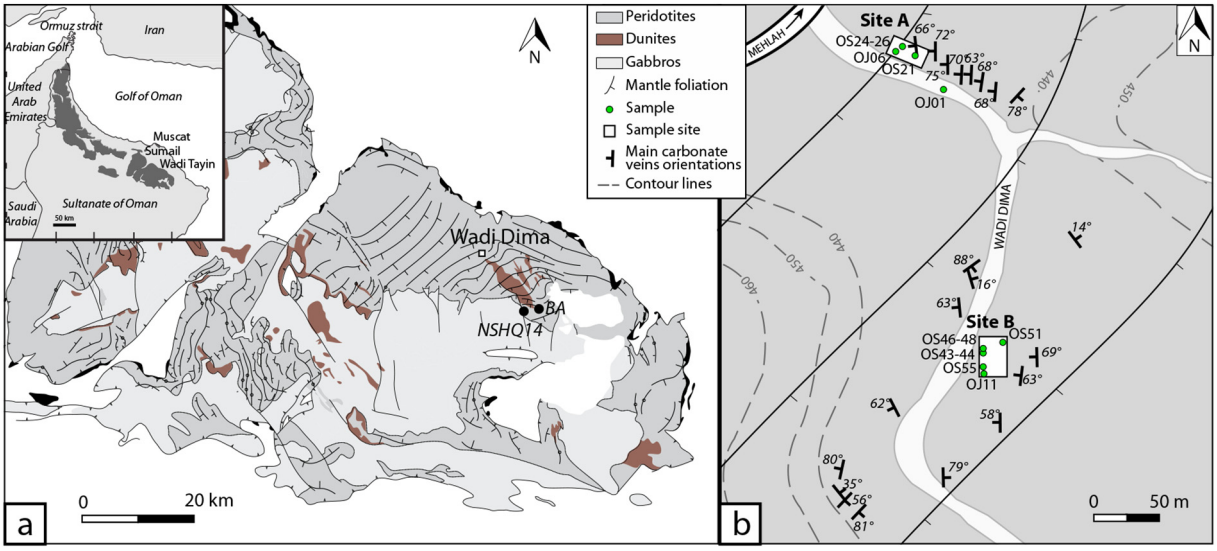

Fig. 1. (a) Map of the Wadi Tayin massif (after Nicolas et al., 2000). In inset, location of the Oman Ophiolite in the Sultanate of Oman and the United Arab Emirates Sultanate (from Einaudi et al., 2000). The location of the studied area, Wadi Dima, is indicated together with the location of ICDP Site BA (Oman Drilling Project 2017-2018) and of Well NSHQ14 (Ministry of Water Resources of the Sultanate of Oman); (b) Structural map of the studied Wadi Dima area (UTM coordinates 2,542,255 m N and 663,354 m E in zone 40 Q) with the location of studied Sites A and B and of the analyzed samples (OS21-55=15OS21-55; OJ01-11=17OJ01-11). The orientation of the carbonate veins and of the peridotite foliation in the vicinity of Sites A and B is indicated.

which now comprise the Jebel Akhdar, the highest mountain in the Sultanate of Oman (3075 m). The Hawasina and continental carbonate formations appear as tectonic windows between ophiolitic massifs.

Recent high-precision Pb dating by Rioux et al. (2016 and references therein) documents the timing of the transition from ridge accretion to subduction. Oceanic accretion occurred from 96.12-95.50 Ma and was rapidly followed by the onset of convergence from 95.29-95.08 Ma. A diachronous development of the metamorphic sole occurs between the northern massifs (96.16 Ma; Sumeini) and southern massifs (94.81 Ma; Wadi Tayin) but the ophiolite was exhumed synchronously. Ophiolite emplacement onto the Arabian continental margin continued until 78-71 Ma (Late Campanian Juweiza Formation; Rabu et al., 1993). During this period, the ophiolite was alternatively under shallow seawater or emerged above sea level during transgression-regression cycle. During the Oligocene to early Miocene, uplift and erosion exposed the Oman Ophiolite at the paleo-seafloor and formed coarse-grained conglomerates now exposed along wadis (Coleman, 1981; Glennie et al., 1973).

The Oman mantle section comprises mainly harzburgites and minor dunites, which are partially to completely serpentinized (30 to 60%, occasionally up to 100% in low relief areas; Boudier et al., 2009; Kelemen et al., 2011). High temperature carbonatized peridotites (listvenites) are observed at the base of the ophiolitic mantle section (Falk and Kelemen, 2015). They were formed during subduction after reaction with sediment-derived fluids. Carbonatization is also observed in association with peridotite-hosted alkaline springs as low temperature carbonates veins and travertine terraces (Clark et al., 1992; Clark and Fontes, 1990; Falk et al., 2016; Kelemen et al., 2011; Mervine et al., 2014). Fluids forming low temperature carbonates record at least three stages of fluid-rock interaction (Barnes et al., 1978; Chavagnac et al., 2013a, 2013b; Dewandel et al., 2005; Kelemen et al., 2011; Neal and Stanger, 1985; O'Neil and Barnes, 1971; Paukert et al., 2012; Weyhenmeyer et al., 2000):

(i). Meteoric water (in equilibrium with atmosphere) reacts with the weathered mantle at the surface and these reactions produce Mg-HCO_3 water;
(ii). Mg-HCO_3 water infiltrates and interacts with the mantle basement at depth, in a closed system (no longer in equilibrium with atmosphere). These reactions produce serpentine, magnesite, dolomite and calcite and deep groundwater having high pH and typified by Ca–OH-rich, carbon-poor compositions;
(iii). Alkaline springs form as the high pH groundwater reaches the surface and rapidly reacts with atmospheric CO_2 to precipitate calcite-rich travertines.

We focused our study on the Wadi Dima area (UTM coordinates 2,542,255 m N and 663,354 m E in zone 40 Q; Fig. 1a and b) in the southernmost massif of the Oman Ophiolite, Wadi Tayin massif (Fig. 1a and b). The Wadi Dima area is located 10-15 km to the NW of Site BA of ICDP-Oman Drilling Project (OmanDP, Kelemen et al., 2013; Fig. 1a). It exposes a 200 m x 400 m planar surface of partially altered to highly altered harzburgites cross-cut by high density carbonate vein networks (Figs. 1b and 2). This studied area is locally concealed by conglomerates, and surrounded by moderately serpentinized harzburgites that show no evidence of carbonatization in the field. After structural mapping and measurements of the mantle foliation and of the spatial distribution of harzburgite hosted carbonate veins, we selected two sites for detailed petro-structural and geochemical study, located approximately 100-200 m from each other (Fig. 1b). Site A is a 30°SW dip planar surface (50 m x 10 m) and Site B is a nearly horizontal planar surface (100 m × 10 m) traversed by the wadi (forming locally vertical exposures). The two sites exhibit highly serpentinized harzburgites hosting abundant carbonates with different microstructures and morphologies (Fig. 2). Here we report results obtained on twelve 10-20 cm long 4 cm diameter cores of highly serpentinized harzburgites hosting carbonates; 5 cores were collected at Site A and 7 cores were collected at Site B (Supplementary Table A). In addition, two less altered harzburgites were sampled at Site A and B to determine the microstructures (foliation and lineation) of the mantle exposed in Wadi Dima.

3. Methods

The microstructures, petrography and geochemistry of Wadi Dima samples were measured using different analytical techniques, as summarized thereafter. Sample preparation, analytical protocols, operating conditions and data reduction procedures are further detailed in the Supplementary Material.

The microstructures of the carbonates and serpentinized carbonate-bearing harzburgites were measured using High Resolution X-ray

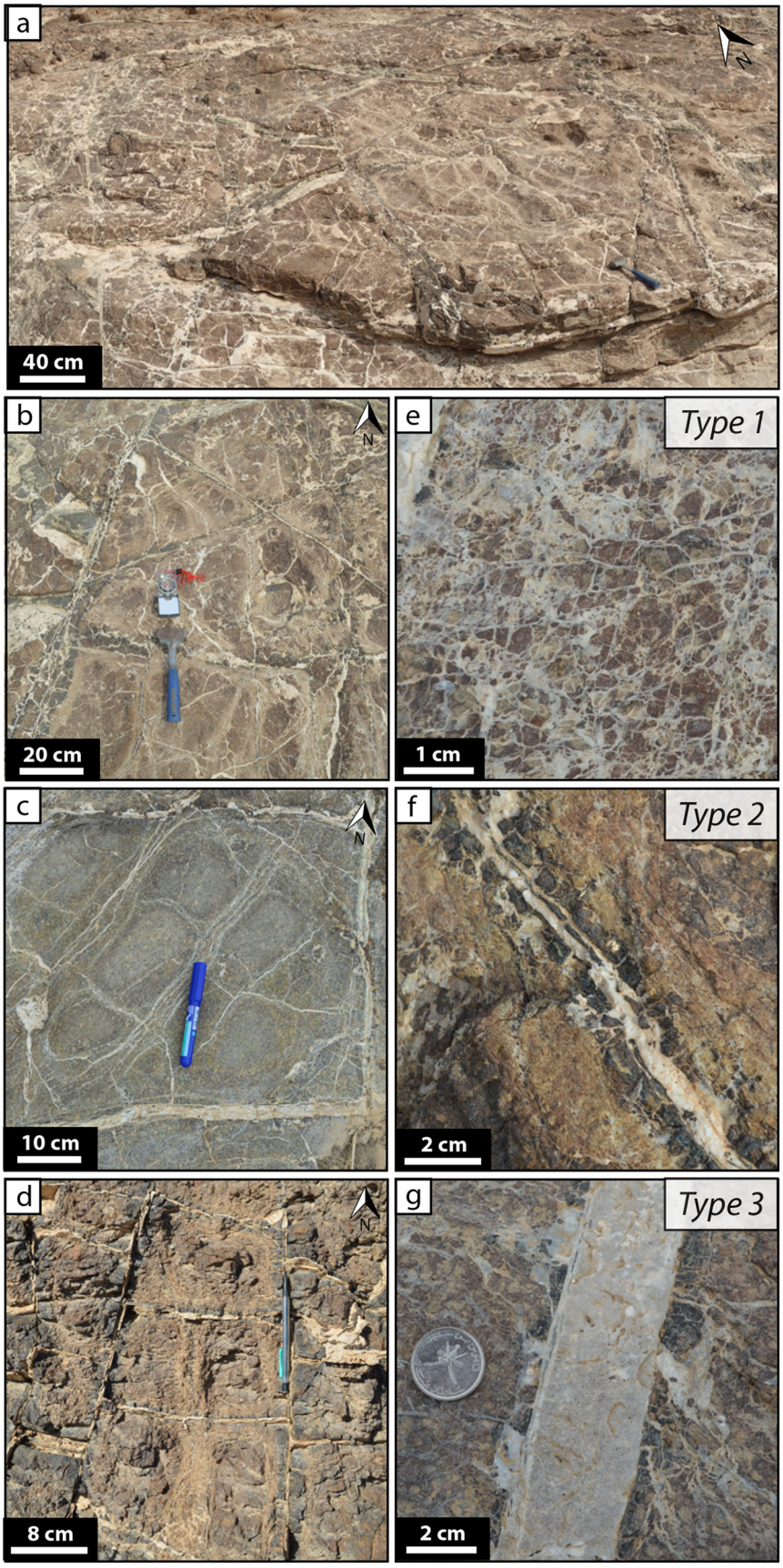

Fig. 2. (a-d) Photographs of harzburgite-hosted carbonate vein networks showing vein density and field relationships and morphologies at different scale, in the Wadi Dima area. Photographs of the three types of carbonate veins distinguished in the field: (e) Type 1: fine (50 to 200 μm) discontinuous penetrative veinlets in the serpentine matrix; (f) Type 2: wide (0.2 to 1 cm) carbonate veins bounded by 0.1 to 2 cm serpentinized selvages; (g) Type 3: wide (0.5 to 2.5 cm) carbonate vein reactivating Type 2 carbonate veins.

Table 1
Major elements compositions (wt%) of harzburgite-hosted carbonates in Wadi Dima area, Wadi Tayin Massif.

Sample	15OS21	15OS44	15OS21	15OS25	15OS21	15OS44	15OS21	15OS44	15OS26	15OS26	17OJ06
Type	1	1	1	1	2	2	2	2	3	3	3
Microtexture	Core	Core	Veinlet	Veinlet	Large crys.	Large crys.	Microcrystals	Microcrystals	Large crys.	Microcrystals	Microcrystals
SiO_2	0.03	0.03	0.06	0.03	0.02	0.00	0.03	0.11	0.18	0.08	0.06
FeO	0.31	0.39	0.17	0.19	0.03	0.00	0.00	0.01	0.01	0.03	0.00
MnO	0.09	0.00	0.08	0.16	0.07	0.01	0.01	0.03	0.31	0.03	0.01
MgO	0.38	11.99	0.01	11.30	0.30	3.36	20.28	7.53	0.07	17.50	14.95
CaO	52.08	35.27	48.13	37.18	58.30	46.72	38.16	35.53	43.88	36.87	35.34
Total	52.90	47.68	48.44	48.86	58.72	50.08	58.48	43.21	44.45	54.51	50.36
Recalculated numbers of ions on the basis of 6Ox											
Fe	0.01	0.01	0.01	0.01	0.00	0.00	0.00	0.00	0.00	0.00	0.00
Mn	0.00	0.00	0.00	0.00	0.00	0.00	0.00	0.00	0.01	0.00	0.00
Mg	0.02	0.64	0.00	0.59	0.01	0.18	0.85	0.45	0.00	0.80	0.74
Ca	1.97	1.35	1.99	1.40	1.98	1.82	1.15	1.54	1.98	1.20	1.26
Total	2.00	2.00	2.00	2.00	2.00	2.00	2.00	2.00	2.00	2.00	2.00
Mg/Ca	0.01	0.47	0.00	0.42	0.01	0.10	0.74	0.29	0.00	0.66	0.59

microtomography (HR-XCT, European Synchrotron Radiation Facility (ESRF), Grenoble, France) and electron backscattered diffraction (EBSD, CamScan CrystalProbe X500FE Scanning Electron Microscope (SEM), service de Microscopie Électronique et Analytique (MEA), University of Montpellier, France) on minicores and polished thin sections respectively. Thin sections were cut, atop the cores drilled in the field, below and parallel to the weathered surface. Mini-cores (1.7 mm diameter x 5 mm long) were drilled on the outer surface of core sample 15OS46 (Site B) with a special focus on transition from carbonate veins to serpentinized harzburgites. HR-XCT images were acquired with a 0.65 μm resolution on the ID19 beamline (ESRF) and 3D images were reconstructed using pyHST (Mirone et al., 2014) then processed for visualization using Avizo® software. EBSD images and microstructures data were study on thin sections. Carbonates were analyzed on samples 15OS21, -26 and -44. The crystallographic preferred orientation (CPO) of olivine was measured in two of the least altered harzburgites sampled in the studied areas, harzburgites 17OJ01 (Site A) and 17OJ11 (Site B; Fig. 1b). Images (EBSD maps) and microstructures data were processed using CHANNEL5 software from Oxford Instruments HKL and using MTEX®, an open-source MatLab® toolbox (Mainprice et al., 2015).

The petrology of the carbonates and serpentines in serpentinized carbonate-bearing harzburgites was identified on uncoated polished thin sections using a cold-cathode CITL 8200 Mk5-1 Optical Cathodoluminescence (CL) Microscope Stage coupled to an Olympus BX41 optical microscope (at Geosciences Montpellier, University of Montpellier), operating at 15 kV and 250 μA, and using RAMAN spectroscopy Renishaw Invia (at Charles Coulomb Laboratory, University of Montpellier) on two samples (15OS44, -21). RAMAN cartography was made using a laser with a wavelength of 633 nm and a power of 7.6 mW, coupled with an open microscope equipped with a 50 objective (Leica N Plan). Acquisition time was 0.4 sec. The spectral region investigated was from 3500 to 3900 cm^{-1}.

The major element composition of minerals composing the serpentinized harzburgites and carbonate veins was determined on 8 samples by Electron Probe Micro-Analyser (EPMA) at the Service Microsonde Sud (University of Montpellier), using a CAMECA SX100 equipped with five wavelength-dispersive X-ray spectrometers (WDS). Analyses were done with 20 kV accelerating potential, 10 nA beam current and 30 s counting times for all elements measured. Natural minerals and synthetic oxides are used as standards. Major elements are reported in Table 1 and Supplementary Table B.

A subset of 6 samples was analyzed for trace element concentrations at Geosciences Montpellier (France) using a Thermo Scientific Element 2 XR (eXtended Range) high resolution - Inductively Coupled Plasma Mass Spectrometer coupled with a GeoLas Q + Excimer laser ablation system (CompEx102 laser from LambdaPhysik) (LA-ICPMS). The laser energy conditions were set to 12^{-15} J cm^2 and 7 Hz and the beam size was set to 102 μm. Data were processed using Glitter Software (Griffin et al., 2008); concentrations were calibrated using standard synthetic NIST612 glass (Pearce et al., 1997) and internal standardization relative to ^{43}Ca compared to EPMA values. The precision and accuracy of the LA-ICP-MS analyses and the values obtained for standard reference basalt BIR-1G are detailed in Supplementary Material. Trace element compositions are reported in Table 2 and Supplementary Table C.

Two harzburgites from Site A (15OS21,-24) and four harzburgites from Site B (15OS43, -44, -48, -55) were selected for bulk rock carbon and oxygen isotope analyses in carbonates. 17 zones of interest were microdrilled in the carbonate veins (3.8 mm diameter and 5 mm length) then crushed in agate mortar. This "micro-bulk" rock sampling approach was used in order to sample the different types of carbonates. Oxygen and carbon isotope compositions were measured using a Thermo-Fisher Delta V continuous-flow IRMS GasBench with an on-line chemical separation of calcite- and dolomite-derived CO_2 at IPGP (France). Data were corrected using standard linearity mass equation and standard real value correction. Six internal standards of pure calcite (RII, A, M) and pure dolomite (Cri, Ml, T) were used to calibrate isotopic composition. Internal standards were calibrated against IAEA standards: NBS19 and IAEA-CO-1.The mean accuracy of this method is 0.058‰ for $\delta^{13}C_{V\text{-}PDB}$ and 0.075‰ for $\delta^{18}O_{SMOW}$. Micro-bulk isotopic compositions are reported in Table 3 and Supplementary Table D. using conventional δ notation versus SMOW for oxygen isotope and versus V-PDB for carbon isotope.

In situ oxygen and carbon isotopes compositions of carbonates in epoxy-mounted thin section pieces from seven harzburgites (15OS21, -25, -26, -44, -46, -55 and 17OJ06) were determined using SHRIMP SI at the Australian National University (Ireland et al., 2008). Carbon and oxygen isotope analyses ($\delta^{13}C$, $\delta^{18}O$) were conducted on the same or very similar spot locations over two separate sessions. Measurements were conducted with a 3.5 nA Cs^+ primary beam and a spot size of 25-30 μm. An electron gun was used to provide a defocused electron beam to minimize charging of the insulating target surface. Multi-collector isotope ratio measurements were conducted using two Faraday cups on moving heads. Data were reduced using POXI-MC software (software developed specifically for reduction of SHRIMP data by Peter Lanc, ANU). Reduction included background subtraction, correction for Electron-Induced Secondary Ion Emission (EISIE; correction only relevant for oxygen isotope measurements: see Ickert et al., 2008) standardization and correction for IMF drift within the session. IAEA calcite standards NBS18 ($\delta^{18}O_{SMOW}$ = 7.10‰; $\delta^{13}C_{V\text{-}PDB=}$ -5.01‰; Verkouteren and Klinedinst, 2004) and NBS19 ($\delta^{18}O_{SMOW}$ = 28.65‰; $\delta^{13}C_{V\text{-}PDB=}$ 1.95‰; Verkouteren and Klinedinst, 2004) and one dolomite standard DOL calibrate against IAEA standards ($\delta^{18}O_{SMOW}$= 21.36‰; $\delta^{13}C_{V\text{-}PDB=}$ -0.25‰; personal communication

Table 2
Trace element compositions (ppm) of harzburgite-hosted carbonates in Wadi Dima area, Wadi Tayin Massif.

Date	27/10/16	29/03/17	29/03/17	29/03/17	29/03/17	29/03/17	08/12/16	29/03/17	08/12/16	29/03/17	29/03/17	29/03/17	16/03/17	16/03/17
Sample	150S21	150S21	150S25	150S44	150S46	150S21	150S44	150S44	150S44	150S44	150S46	150S25	150S26	150S26
Type	1	1	1	1	1	2	2	2	2	2	2	3	3	3
Microtexture	Core	Veinlet	Veinlet	Veinlet	Veinlet	Large crys.	Large crys.	Large crys.	Microcrystals	Microcrystals	Microcrys.	Large crys.	Microcrys.	Microcrys.
CaO (wt%)	50	52	35	45	40	50	44	50	38	40	38	50	34	34
SiO_2 (wt%)	6.15	1.96	1.43	0.53	1.20	0.15	0.04	0.11	0.35	0.39	0.88	0.88	0.71	1.97
Sc	1.53	0.70	1.07	b.d.	0.40	0.08	0.02	b.d.	0.22	0.11	0.24	0.58	0.28	0.29
Ti	29.92	3.13	7.57	17.78	18.84	0.29	1.39	13.73	30.04	13.49	9.26	3.01	3.27	11.45
V	20.66	2.48	0.83	0.34	1.75	0.02	0.18	0.15	0.85	0.48	0.89	0.54	0.91	1.43
Cr	90.6	6.7	9.7	6.5	10.2	8.3	5.8	10.2	15.6	11.3	8.6	12.3	6.6	10.1
Mn	487	359	258	803	255	30	232	18	72	36	261	68	95	262
Co	17.9	11.8	3.9	4.7	13.2	1.5	0.2	0.6	1.3	1.5	11.3	1.5	3.0	2.3
Ni	623.8	105.7	79.5	41.7	59.9	3.8	0.5	2.6	10.1	9.7	69.9	54.2	49.1	110.4
Cu	13.96	1.69	2.00	0.60	1.40	0.44	0.14	1.22	1.44	3.14	1.71	2.00	1.14	1.77
Zn	17.81	2.14	4.83	1.09	2.16	1.47	0.14	0.48	1.25	0.93	3.72	11.92	1.63	4.00
Rb	b.d.	0.035	0.075	b.d.	0.226	b.d.	0.012	0.076	0.376	0.233	0.100	0.040	0.057	0.195
Sr	310	681	380	930	1941	1213	456	507	575	654	1770	1340	200	401
Y	0.032	0.122	0.196	0.479	0.471	0.136	0.445	0.434	0.995	2.007	0.711	1.160	0.080	0.241
Zr	0.012	0.038	0.483	0.781	0.383	0.022	0.017	0.109	0.914	0.260	0.161	0.071	0.144	0.148
Nb	0.002	0.002	0.017	0.005	0.025	0.004	0.001	0.045	0.079	0.030	0.016	b.d.	0.004	0.018
Sb	0.295	b.d.	b.d.	b.d.	b.d.	0.003	b.d.	0.013	0.009	0.022	b.d.	b.d.	b.d.	b.d.
Ba	10.1	12.8	10.4	25.5	32.4	19.5	17.5	39.3	39.2	42.3	45.7	22.1	3.0	15.2
La	0.041	0.107	0.088	0.242	0.329	0.148	0.040	0.050	0.355	0.134	0.539	1.038	0.134	0.278
Ce	0.022	0.072	0.113	0.277	0.556	0.030	0.065	0.099	0.662	0.395	0.927	0.623	0.222	0.373
Pr	b.d.	0.022	0.017	0.058	0.074	0.026	0.013	0.008	0.088	0.040	0.124	0.225	0.028	0.062
Nd	0.016	0.087	0.044	0.224	0.259	0.101	0.080	0.028	0.381	0.185	0.477	0.951	0.122	0.246
Sm	b.d.	0.011	b.d.	0.039	0.055	0.019	0.022	b.d.	0.092	0.058	0.098	0.194	0.021	0.041
Eu	b.d.	0.003	0.002	0.014	0.007	0.005	0.007	0.001	0.024	0.014	0.017	0.048	0.005	0.008
Gd	0.022	0.018	b.d.	0.076	0.052	0.022	0.060	0.012	0.159	0.074	0.114	0.258	0.022	0.037
Tb	b.d.	0.003	0.003	0.012	0.009	0.003	0.006	0.003	0.017	0.016	0.015	0.027	0.003	0.005
Dy	b.d.	0.015	0.026	0.068	0.040	0.022	0.045	0.013	0.132	0.139	0.100	0.208	0.014	0.033
Ho	b.d.	0.003	0.004	0.008	0.010	0.003	0.008	0.006	0.027	0.036	0.019	0.041	0.003	0.007
Er	b.d.	0.010	0.017	0.044	0.033	0.008	0.030	0.022	0.075	0.126	0.057	0.091	0.007	0.021
Tm	b.d.	0.001	0.002	0.003	0.004	0.001	0.005	0.004	0.008	0.021	0.007	0.015	0.001	0.003
Yb	b.d.	0.010	0.020	b.d.	0.032	0.009	0.029	0.019	0.061	0.106	0.062	0.076	0.007	0.017
Lu	0.004	0.002	0.004	0.004	0.006	0.001	0.004	0.002	0.012	0.017	0.009	0.013	0.001	0.004
Hf	b.d.	b.d.	0.009	b.d.	0.013	b.d.	b.d.	b.d.	0.026	b.d.	b.d.	b.d.	0.004	b.d.
Ta	b.d.	b.d.	0.011	b.d.	0.003	0.001	b.d.	0.003	0.006	0.002	0.001	b.d.	0.001	0.002
Pb	5.150	0.019	0.066	0.053	0.320	0.021	0.022	0.120	0.122	0.222	0.555	0.595	0.027	0.164
Th	0.006	0.005	0.030	0.010	0.031	0.002	0.004	0.010	0.103	0.040	0.027	0.005	0.039	0.028
U	0.058	0.018	0.014	0.020	0.032	0.000	0.030	0.005	0.035	0.010	0.017	0.011	0.011	0.014

Table 3
"Micro-bulk-rock" oxygen and carbon isotopic compositions (V-PDB and SMOW) and calculated temperatures T_{ca} and T_{dol} (using equation from Friedman and O'Neil, 1977 and Matthews and Katz, 1977) of harzburgite-hosted carbonates in Wad Dima area, Wadi Tayin Massif.

	Sample	15OS21	15OS43	15OS48	15OS55	15OS43	15OS44	15OS48	15OS55	15OS21	15OS24	15OS48
	Type	1	1	1	1	2	2	2	2	3	3	3
CALCITE	$\delta^{13}C_{v\text{-}pdb}$	-7.26	-6.85	-7.39	-7.52	-7.20	-7.29	-7.94	-6.24	-7.61	-6.69	-7.05
	std. dev.	0.061	0.035	0.040	0.069	0.088	0.061	0.062	0.103	0.105	0.043	0.017
	$\delta^{18}O_{v\text{-}pdb}$	-2.52	-3.61	-2.08	-3.22	-1.39	-1.16	0.79	-1.12	-1.91	-0.91	1.01
	$\delta^{18}O_{SMOW}$	29.13	27.13	28.71	27.54	29.42	29.67	31.68	29.71	28.89	29.92	31.90
	std. dev.	0.032	0.037	0.027	0.059	0.035	0.036	0.044	0.028	0.112	0.072	0.035
	T_{ca}	18	27	19	25	16	15	7	15	18	14	6
DOLOMITE	$\delta^{13}C_{v\text{-}pdb}$	-7.72	-7.11	-7.45	-8.42	-7.36	-7.47	-8.77	-7.76	-7.86	-7.11	-7.72
	std. dev.	0.031	0.105	0.056	0.055	0.064	0.039	0.025	0.082	0.031	0.049	0.043
	$\delta^{18}O_{v\text{-}pdb}$	-8.97	-11.66	-12.79	-12.34	-3.96	-0.22	1.73	-0.51	-0.73	1.76	1.39
	$\delta^{18}O_{SMOW}$	21.61	18.84	17.68	18.14	26.78	30.63	32.65	30.33	30.11	32.67	32.29
	std. dev.	0.049	0.170	0.058	0.086	0.050	0.076	0.038	0.067	0.029	0.050	0.036
	T_{Dol}	72	92	101	97	41	23	15	25	26	15	17

from I. Williams) were measured during these sessions. NBS19 and NBS18 were used as the principal reference material for oxygen and carbon measurements respectively. NBS19 exhibited a repeatability of ±0.087‰ (2SE) and ±0.90‰ (2SD) for $\delta^{18}O_{SMOW}$ and NBS18 of ±0.45‰ (2SE) and ±1.79‰ (2SD) for $\delta^{13}C_{V\text{-}PDB}$. Correction for bias in measured $\delta^{18}O$ due to a matrix effect correction between calcite and dolomite was applied using a calibration previously developed at ANU (with a matrix bias relative to calcite of: -0.283*wt.% MgO + 0.2485 ‰; personal communication from I. Williams and C. Kooymans). *In situ* isotopic compositions are reported in Table 4 and Supplementary Table E.

4. Results

4.1. Field relationships and structural overview of the Wadi Dima area

The Wadi Dima sites expose, over large flat surfaces, a suite of partially to highly serpentinized harzburgites, the most altered samples being cross-cut by abundant carbonate veins (Fig. 2). The crystallographic preferred orientations (CPO) of olivine were measured in the least altered harzburgites and show a strong axial (010) [100] fabric (Fig. 3b and d), which is typically related to asthenospheric mantle flow (Boudier et al., 2009; Boudier and Coleman, 1981; Nicolas, 1989). Mantle foliation (010)ol is oriented ~N15E/80° in Site A and ~N185E/80° (strike and dip RHR notation) in Site B and mantle lineation [100]ol is dominantly sub-horizontal in this area, trending N-S to NNE-SSW. The measured CPO are overall consistent with the regional mantle foliation determined by Nicolas et al. (2000); (Fig. 1b).

Carbonates outcrop as 0.5 mm to 8 cm wide veins forming, at the meter scale, high density, often orthogonal, networks (Fig. 2a-d). In the field, we distinguished three types of carbonates on the basis of their field relationships and morphologies (Fig. 2e-g).

Type 1 carbonates are thin (50 to 200 μm) carbonate veinlets observed pervasively throughout the highly serpentinized harzburgites. They have random orientations (Fig. 2e).

Type 2 carbonates are pluri-mm thick veins (0.2 to 1 cm) delimited by cm-thick serpentine selvages (Fig. 2f). The later are in turn crosscut by carbonate veinlets, taking root in Type 2 veins and connecting with Type 1 carbonate network (Fig. 2b-d).

Type 3 carbonates are pluri-mm to cm thick veins (0.4 to 2.5 cm). They have no serpentine selvages and they appear to reactivate Type 2 carbonate veins (Fig. 2g).

Looking to their spatial distributions, both Type 2 and 3 carbonate veins are characterized by three main (or dominant) orientation clusters, which are variously prominent in the field (Fig. 3a and c). Two of the preferentially oriented vein groups are sub-vertical and they appear to be related to olivine CPO (Fig. 3b and d): the first vein group is parallel to the (010)ol slip plane (striking NNE-SSW) while the second vein group is sub-orthogonal to [100]ol and [001]ol slip directions. The third group is defined by sub-horizontal veins. It is poorly represented in Type 2 carbonates veins, but it is dominant in Type 3 veins, particularly at Site B. This relative abundance at Site B could be a measurement bias due to the locally vertical topography of Site B, where cross-cut by the wadi.

4.2. Microstructures and mineralogy of harzburgite-hosted carbonates

The carbonate-bearing harzburgites are highly to completely serpentinized and minor relics of orthopyroxene and spinel were identified only in a few samples. They are composed dominantly of serpentine and bastite formed after olivine and pyroxene respectively, Fe-oxides (magnetite) and carbonates. Serpentine is lizardite with minor chrysotile and displays typical mesh texture.

Type 1 carbonate veins are discontinuous and penetrative: they follow the lizardite mesh and cleavages in the altered pyroxenes (Fig. 4a and b). HR-XCT imaging reveals that Type 1 veinlets are associated to 10 to 150 μm carbonate cores (Fig. 4c-e). These carbonate cores are located in the center of the mesh texture rimed by Fe rich amorphous proto-serpentine phase (APSP) from which crystalize chrysotile and polygonal serpentine (Andreani et al., 2007; Plümper et al., 2012; Fig. 5).

Table 4
In-situ oxygen and carbon isotopic compositions (V-PDB and SMOW) using SHRIMP-SI and calculated temperatures $T_{ca/dol}$ (using equation from Friedman and O'Neil, 1977 and Matthews and Katz, 1977) of harzburgite-hosted carbonates in Wad Dima area, Wadi Tayin Massif.

Sample	15OS44	15OS44	15OS21	15OS46	15OS21	15OS21	15OS21	15OS44	15OS25	17OJ06	17OJ06
Type	1	1	1	1	2	2	2	2	3	3	3
Microstructure	Core	Core	Veinlet	Veinlet	Large crys.	Large crys.	Microcrys.	Microcrys.	Microcrys.	Microcrys.	Microcrys.
MgO (wt%)	0.17	0.61	1.39	1.33	0.17	0.12	19.04	5.92	19.12	18.72	20.55
$\delta^{13}C_{v\text{-}pdb}$	-15.2	-4.6	-11.9	-6.2	-4.0	-9.3	-10.4	-6.8	-7.8	-7.3	-8.3
2σ error	0.63	0.63	0.85	0.59	0.70	0.62	0.79	0.62	0.73	0.75	0.62
$\delta^{18}O_{SMOW}$	27.4	26.5	28.2	26.0	28.2	28.4	29.4	27.8	30.2	30.8	32.2
2σ error	0.13	0.11	0.11	0.11	0.12	0.12	0.11	0.11	0.12	0.14	0.13
$T_{ca/dol}$	25.41	30	22	32	21	21	29	24	25	23	17

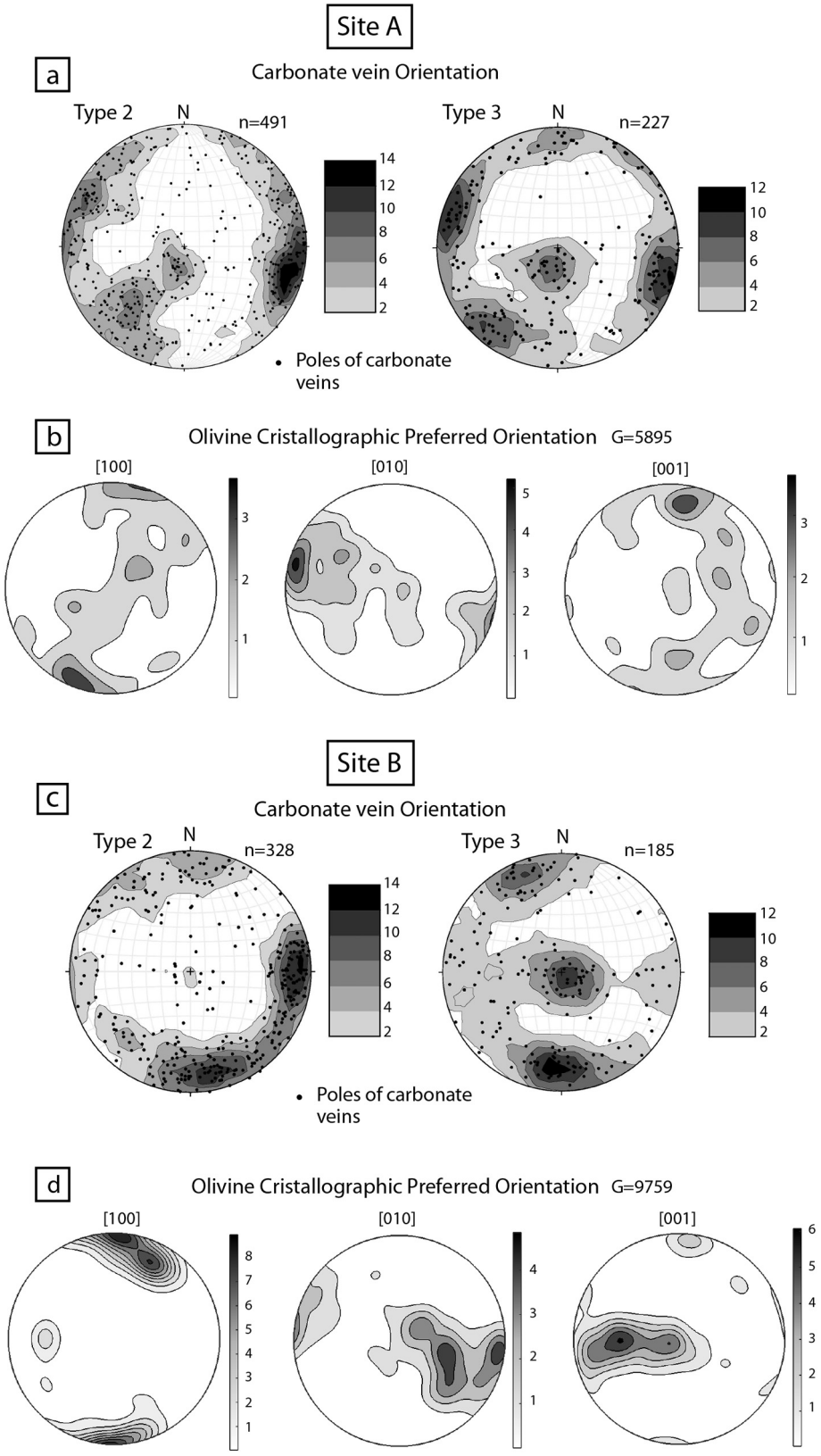

Fig. 3. Lower hemisphere equal area projections of: (a) harzburgite-hosted carbonate veins plotted as poles to planes, Kamb contours (interval: 2% area; n is the number of measurements). Measurements were taken on 30° dip planar surface (50 m × 10 m). (b) olivine crystallographic orientations (Electron backscatter diffraction – EBSD analyses; G is the number of olivine grains measured) of sample 17OJ01 at Site A. (c) harzburgite-hosted carbonate veins plotted as poles to planes, Kamb contours (interval: 2% area; n is the number of measurements). Measurements were taken on a nearly horizontal planar surface (100 m x 10 m). (d) Olivine crystallographic orientations (EBSD analyses; G is the number of olivine grains measured) of sample 17OJ11 at Site B.

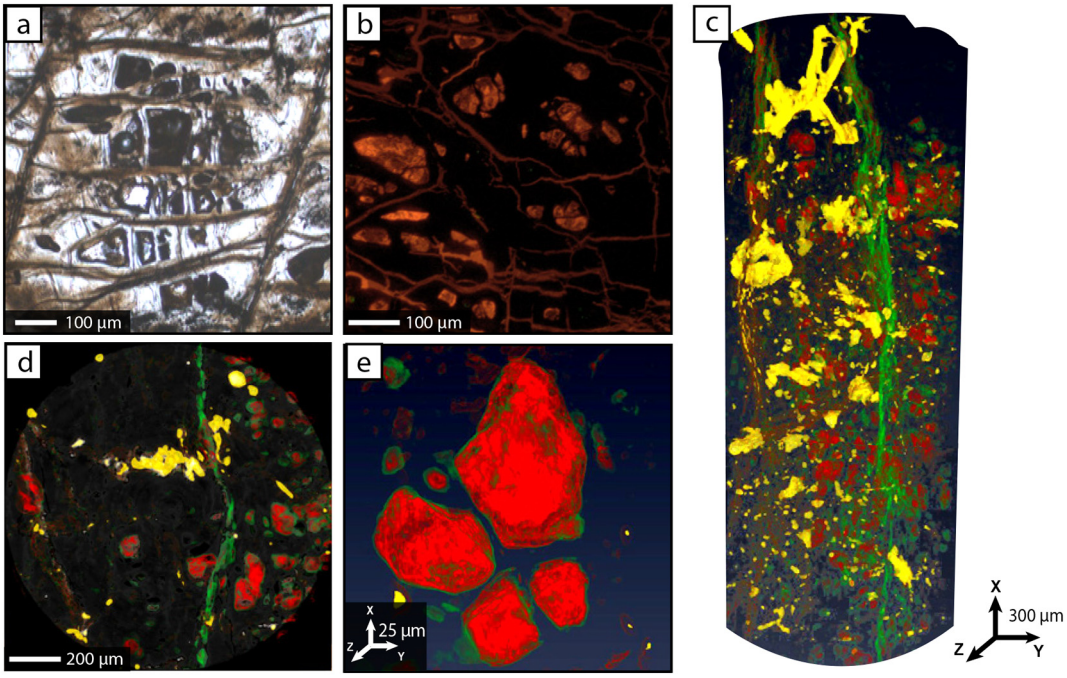

Fig. 4. Microtexture of Type 1 carbonates. (a-b) Microphotography (plane-polarized light; PPL) and Cathodoluminescence (CL) images of the serpentinized matrix showing 20 to 150 µm carbonate cores and 10 to 30 µm veinlets (15OS44 sample) (c-e) X-ray microtomography of carbonate veinlets and cores (sample 15OS21), processed by Avizo software; (c) 3D image of the core showing oxides and spinels (yellow), carbonate veinlet (green) and carbonate cores (red); (d) 2D image of a slice (e) 3D image of 50 to 150 µm large carbonate cores

They were formed after olivine. Type 1 carbonates are dominantly calcite with minor dolomite, which is mainly located in carbonate cores (Fig. 6; Table 1).

Type 2 carbonate veins comprise ~50% large calcite crystals and ~50% microcrystals of calcite and dolomite interlayered with 100 to 500 µm serpentine bands. Serpentine grains are observed also as inclusions between carbonate grains (Fig. 7a and b). Microcrystals range in compositions between calcite and dolomite end-members (Fig. 6, Table 1). In samples 15OS21 and 15OS44, Type 2 carbonate veins display highly variable textures, from crack seal to epitaxial and syntaxial textures. Partially to completely recrystallized textures are defined by large elongated calcite crystals (200 × 500 µm) surrounded by late calcite and dolomite microcrystals (<10 µm). Large calcite crystals display strong internal misorientations (up to 9°) indicating the formation of subgrains (Fig. 7c). The presence of subgrains in large calcite crystals and irregular grain boundaries suggests that calcite was deformed by dislocation creep resulting in strain recovery by dynamic recrystallization. Surrounding new microcrystals of calcite and dolomite are neoblasts. They are developed around and at the expense of parent large calcite grains. These newly formed grains do not show evidence of misorientation and they have a relative strong CPO fabric (Fig. 7d). Crack-seal textures are defined by a succession of well-oriented grain layers (strong fabric) alternating with poorly-oriented grain layers (weak fabric; sample 15OS44; Fig. 7e). We note a rotation of 90-100° of c[0001] and a[2110] calcite crystallographic axes between the two intercalated carbonate layers (Fig. 7f). Well-oriented grains are elongated with c-axis [0001] perpendicular to the vein boundaries (syntaxial texture). Poorly-oriented calcite grains have c-axis [0001] parallel to vein boundaries that is parallel to the expected direction of fluid flow (Fig. 7e and f). We interpret the occurrence of these juxtaposed textures as an evidence of a polygenetic formation, with oriented calcite grains crystallizing first during the opening of the crack and poorly-oriented grains crystallizing later during the re-opening of this crack.

Type 3 carbonates are dominantly composed of calcite and dolomite microcrystals surrounding rare large parent calcite crystals (Fig. 8). Minor serpentine is observed as inclusions of <1 to 100 µm between

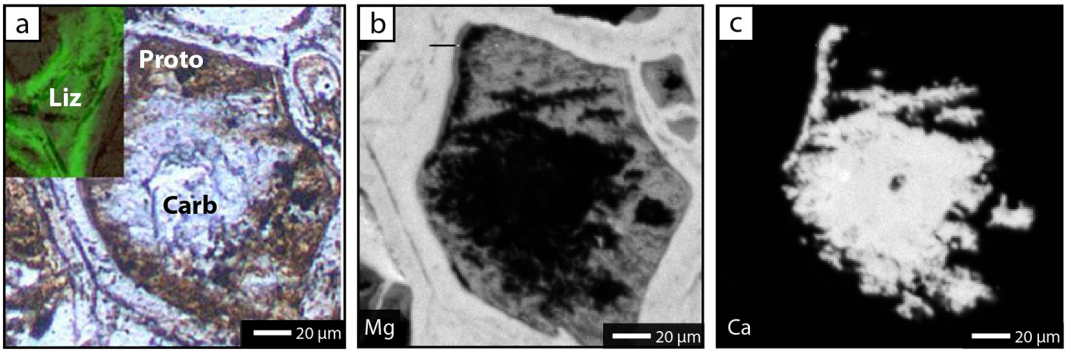

Fig. 5. (a) Microphotography (plane-polarized light; PPL) and RAMAN cartography in inset (b) Element map of Mg (c) Element map of Ca; showing ~120 µm large Ca-rich carbonate core (noted "Carb") surrounded by Mg-poor proto-serpentine (noted "Proto") and lizardite veins (noted "Liz") in a harzburgite (sample 15OS21). Fine grained Fe-oxides are observed in the center of lizardite veins and surrounded carbonate core.

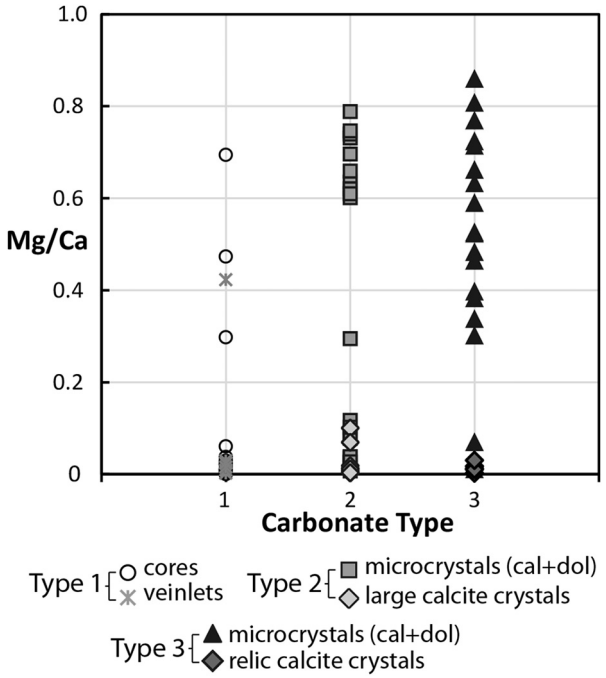

Fig. 6. Cationic Mg/Ca ratios measured in the three carbonate types observed in Wadi Dima. Carbonates have compositions ranging from the calcite to the dolomite end-members.

microcrystals (Fig. 8). Microcrystals have a composition that spreads between calcite and dolomite end-members (Fig. 6; Table 1).

4.3. Trace element geochemistry

The Wadi Dima harzburgite-hosted carbonates have trace element compositions overall similar to that of the hydrothermal carbonates hosted in the oceanic ultramafic sub-seafloor (ODP Site 1274 serpentinized harzburgites and ODP Site 1271 and 1275 gabbro intruded impregnated ultramafic rocks; Bach et al., 2011; Schroeder et al., 2015; Figs. 9 and 10; Table 2). They are slightly enriched in Sr and Ba and significantly depleted in trace elements, in particular Rare Earth Elements (REE) and Y compared to biogenic sedimentary carbonates which are representative of the composition of oceanic carbonate sediments conveyed toward the trench during convergence (global subducting sediment, GLOSS, composition, Plank and Langmuir, 1998; ODP Site 1149; Plank et al., 2007; Fig. 9). The different typ

es of Wadi Dima harzburgite-hosted carbonates display distinct compositions in REE-Y and, to a lesser extent, in chalcophile elements (Pb, Cu and Zn). The distribution of trace element in carbonates depends on their crystallography (e.g., Migdisov et al., 2016), some elements having a stronger affinity for rhombohedral calcite and dolomite (cations with ionic radii smaller than Ca, such as Mn, Fe, Cu, Zn) or for orthorhombic aragonite (larger ionic radii elements, e.g., U, Pb, Ba and Sr). However, these differences in elemental affinities cannot explain the characteristics of the Wadi Dima carbonates (all rhombohedral calcite and dolomite) and we therefore interpreted their trace element geochemistry as characterizing the (variations in) composition of the fluids after which they precipitated.

Type 1 carbonates have low REE-Y concentrations (Yb < 0.2 x C1-chondrite) and they are slightly enriched in U and Y and depleted in Ce relative to neighboring elements ($(Y/Ho)_{CN}$ = 1.3-2.3; $(U/Th)_{CN}$ = 1-13); $(Ce/Ce^*)_{CN}$ = 0.2-1.3; Figs. 9 and 10; Table 2). These fractionations in Ce, Y and U are typically observed in serpentinites and carbonates exposed to extensive interaction with, and precipitating after, seawater-derived fluids (Bach et al., 2011; Schroeder et al., 2015), these anomalies are however less prominent in the Wadi Dima carbonates compared to oceanic hydrothermal carbonates. This suggests that the fluid after which the Wadi Dima carbonates precipitate was modified after fluid-rock interactions. Except for the only carbonate core that we could analyze (from Sample 15OS21), Wadi Dima carbonates have low Cu (0.6-4.6 ppm), Zn (0.9-6.5 ppm) and Pb (0.02-0.3 ppm) abundances. The high Cu, Zn and Pb content of the carbonate core may (1) relate to contamination by the hosting serpentines during analysis, and/or (2) show pore-scale variations in the composition of the fluids after which carbonate precipitates ("micro-environment" effect; Steefel et al., 2005), with a stronger contribution of serpentinization-derived fluids in core carbonates.

Type 2 carbonates display distinct compositions in large crystals and microcrystals. Large calcite crystals have REE-Y and U abundances and patterns similar to that of Type 1 carbonates (Yb < 0.2 x C1-chondrite; $(Y/Ho)_{CN}$ = 1.4-2.8; $(U/Th)_{CN}$ = 0.6-31; Figs. 9 and 10; Table 2). They are distinguished by their lower Zn and Pb abundances (Zn < 1.5 ppm). Type 2 recrystallized calcite and dolomite microcrystals have the highest measured REE-Y abundances (e.g., Yb = 0.4-1 x C1-chondrite; Fig. 10). They display no to little Ce and U fractionation ($(U/Th)_{CN}$ = 0.7-2.3). Type 2 microcrystals have also enriched Pb compositions (Pb = 0.12-0.58 ppm) tending towards that of sedimentary carbonates (Fig. 9). This suggests that the change of texture recorded by Type 2 carbonates occur together with a change in the composition of the fluids after which they precipitated.

Type 3 carbonates are distinguished from Type 1 and 2 carbonates by their Light REE enriched patterns (e.g., La/Yb = 12.1-22.8; Figs. 9 and 10; Table 2) suggesting an increasing control of sorption processes on the REE distribution in fluids as expected at decreasing temperatures (e.g., Bau, 1991). Type 3 carbonates have compositions overlapping that of Type 1 carbonates and Type 2 large calcite for Pb, Sr and Ba but, similar to Type 2 microcrystals, they show no selective enrichments in U. The large calcite relics overlap in composition with Type 2 microcrystals (Yb = 0.30-0.51 x C1-chondrite) and have slightly negative Ce anomalies ($(Ce/Ce^*)_{CN}$ = 0.3-0.5) suggesting slightly oxidized fluids. Calcite and dolomite microcrystals have lower Heavy REE abundances (Yb = 0.04-011 x C1-chondrite) and slight positive Ce ($(Ce/Ce^*)_{CN}$ = 0.6-0.9) anomalies. Such positive Ce anomalies characterize high pH alkaline waters (e.g., Lake Van, Turkey, pH 9.6) and is related to the development of Ce(IV)-carbonate complexes (e.g., Möller and Bau, 1993). This suggests that, similar to Type 2 veins, Type 3 carbonates record a change in the composition and redox of the fluids after which they precipitate during their formation.

We also observed slight to prominent Gd-anomalies in all Wadi Dima carbonates. Gd can become weakly enriched relative to neighboring REE in fluids in presence of carboxylic ligands (Lee and Byrne, 1992), and the development of these Gd anomalies could indicate (a) the occurrence of carbon reduction associated to fluid-rock interaction or (b) an organic carbon rich source for the fluids.

4.4. Oxygen and carbon isotope compositions

Oxygen and carbon isotopes in carbonates are usually used as tracers of mineral precipitation temperatures and fluid sources, respectively, and are commonly analyzed using bulk rock methods (Hoefs, 2008). The oxygen and carbon isotopic compositions of Wadi Dima carbonates were analyzed using two complementary approaches, which allowed characterizing the spatial variability of isotopic compositions in harzburgite-hosted carbonates, from the mm-scale for the micro-bulk-rock approach (Table 3; Fig. 11a and b) down to the μm-scale for in situ isotopic analyses (Table 4; Fig. 11c).

Minimum temperatures of carbonate precipitation were calculated using the thermometers from O'Neil and coworkers (Friedman and O'Neil, 1977) for calcite (noted T_{Ca}) and from Matthews and Katz (1977) for dolomite (noted T_{Dol}). Temperature estimates were calculated by assuming that carbonates precipitate in equilibrium with Oman Ophiolite aquifers ($\delta^{18}O$ = -0.9‰ ± 0.2; Matter et al., 2006; noted

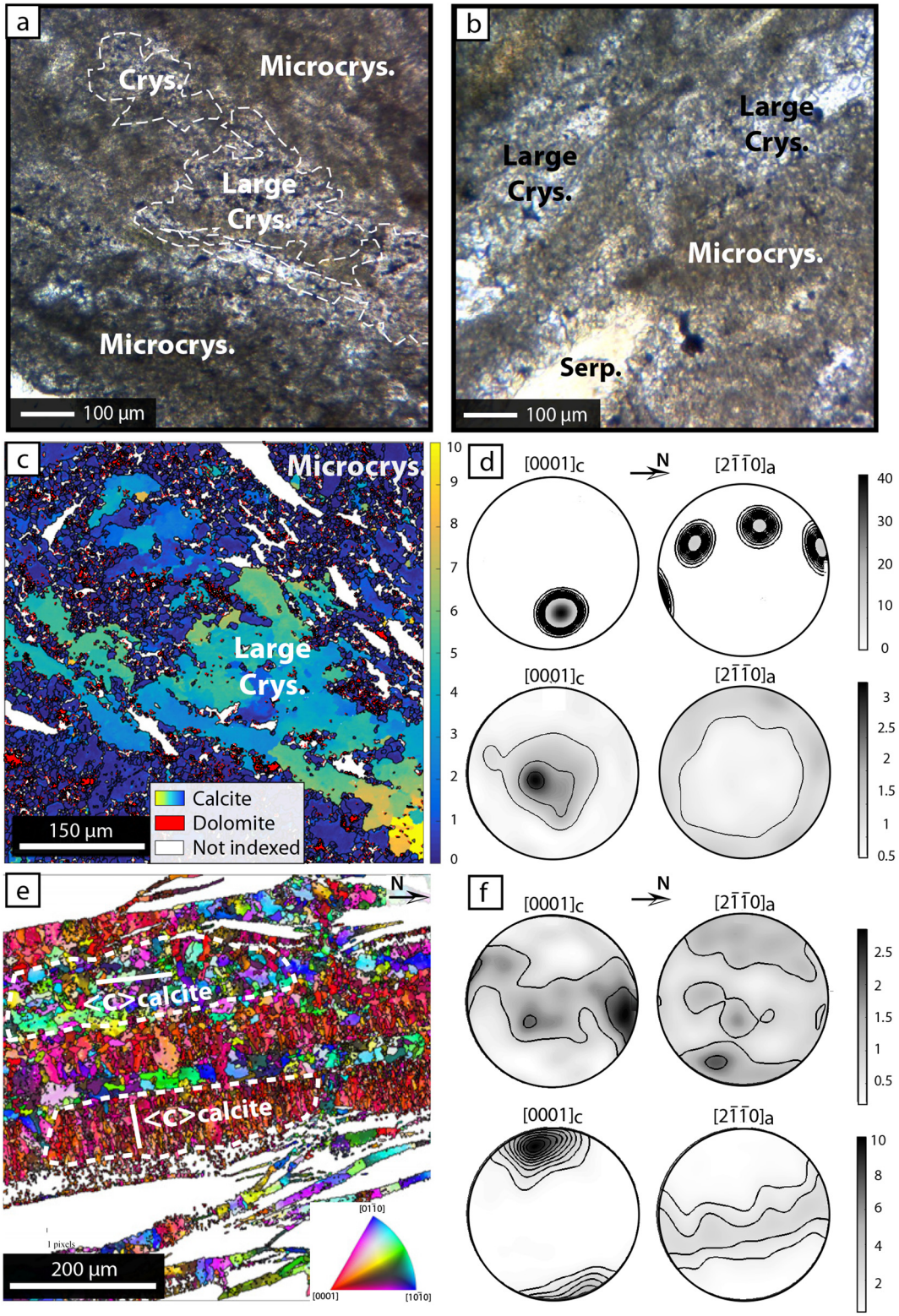

Fig. 7. (a-b) Microphotographs (plane-polarized light; PPL) of 100-500 µm large crystals (noted "Large Crys.") surrounded by a dark area composed of microcrystals (noted "Microcrys.") forming Type 2 carbonate veins (sample 15OS21). Large 200-400 µm serpentine band inclusions (noted "Serp.") are observed; (c) EBSD indexation phase and pattern quality band contrast map representing 200-500 µm large calcite crystal (noted "Large Crys.") surrounded by <10 µm microcrystals of calcite and dolomite (noted "Microcrys."). White spaces correspond to non-indexed phases (mainly serpentine). EBSD map indicates the presence of dolomite in red (<5%) and the angular misorientation of calcite compared to the mean orientation of the grain. Large parent calcite appears color-shaded, indicating a strong internal misorientation (up to 9°) linked to plastic deformation and dynamic recrystallization process. Neoblast calcite microcrystals do not show evidence of internal misorientation; (d) Related EBSD pole figures projections of a-axes and c-axes of the parent large calcite grain and the neoblast calcite microcrystals (number of calcite grains measured = 3923); (e) Inverse Pole Figure (IPF) EBSD map focused on calcite Type 2 carbonate vein (sample 15OS44); (f) Related EBSD pole figures projections. The succession of red grains layers with a growth perpendicular to vein boundaries (c-axis [0001] shows a strong fabric; number of points measured = 22622) with blue-green grains layers showing a weaker fabric (number of points measured = 29692); indicate crack-seal mechanism of formation. Black spaces correspond to non-indexed phases (mainly serpentine). Serpentine phases are included in the red grains layers, close to the vein boundaries.

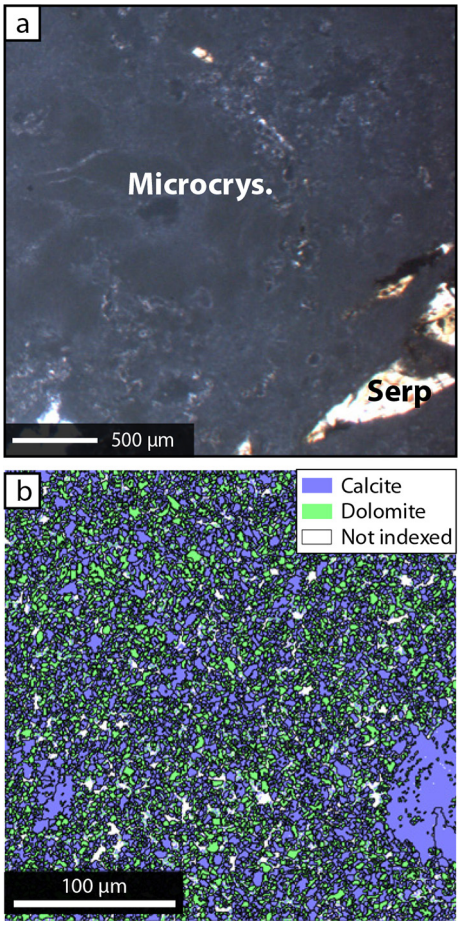

Fig. 8. (a) Microphotography (plane-polarized light; PPL) showing <8 µm microcrystals (noted "Microcrys.") forming Type 3 carbonate veins (sample 15OS26). Note the presence of 300-400 µm wide serpentine band inclusions (noted "Serp"). (b) EBSD phase map representing <8 µm microcrystals of calcite and dolomite and one ~80 µm calcite crystal with corroded rims. White spaces correspond to non-indexed phases (principally serpentine).

$T_{0.9}$), except for Type 1 carbonates for which it was assumed that they could also have been in equilibrium with Cretaceous tropical seawater ($\delta^{18}O$ ~0‰, Pucéat et al., 2003; noted $T_{0.0}$),

As illustrated on Fig. 11, the oxygen and carbon isotopic compositions of the Wadi Dima carbonates overlap that of carbonate veins and travertines measured in the Oman Ophiolite by Clark and Fontes (1990)Clark et al. (1992) and Kelemen et al. (2011). However, as detailed below, the relationships between oxygen and carbon isotopic compositions in the Wadi Dima carbonates differ from that shown by previous bulk geochemical studies.

4.4.1. Micro-bulk compositions

The micro-bulk carbon isotope compositions of the measured Wadi Dima carbonates range from -6.2 to -7.9 ‰ $\delta^{13}C_{V\text{-}PDB}$ for calcite and -8.8 to -7.1 ‰ $\delta^{13}C_{V\text{-}PDB}$ for dolomite (Table 3; Fig. 11a and b). The lighter $\delta^{13}C_{V\text{-}PDB}$ measured in Wadi Dima carbonates indicates a different carbon source and/or a different precipitation process compared to the carbonate veins and travertines previously measured in the Oman Ophiolite. We do not observed differences in carbon isotopic compositions between the three types of Wadi Dima carbonates, which show significant difference in oxygen isotopic compositions.

Type 1 penetrative carbonates have oxygen isotopic composition $\delta^{18}O_{SMOW}$ ranging from 27 to 30‰ for calcite (n = 7), and from 18 to 31‰ for dolomite (n = 7). Precipitation temperatures calculated are $T_{Ca0.0}$ = 20-33°C for calcite and $T_{Dol0.0}$ = 32-109°C for dolomite. The highest calculated temperatures were obtained from analyses of carbonates that were pervasively distributed in the serpentinized harzburgites and correspond to the optically-identified carbonate cores. The precipitation temperatures of dolomite and calcite in Type 1 veinlets ranges from high to low temperatures similar to oceanic hydrothermal carbonates (e.g., Bach et al., 2011; Schroeder et al., 2015; Fig. 11, Table 4). Type 2 carbonate veins have $\delta^{18}O_{SMOW}$ ranging from 29 to 32‰, for calcite (n = 6) and from 27 to 33‰ for dolomite (n = 6), and their calculated precipitation temperatures range from $T_{Ca0.9}$ = 14°C to $T_{Dol0.9}$ = 24°C. Type 3 late carbonate veins have $\delta^{18}O_{SMOW}$ ranging from 29 to 32‰, for calcite (n = 3) and 30 to 33‰ for dolomite (n = 3) and the mean of their calculated precipitation temperatures range from $T_{Ca0.9}$ = 13°C to $T_{Dol0.9}$ = 19°C.

4.4.2. In situ analyses

In situ oxygen and carbon isotope compositions of Wadi Dima carbonates (Table 4) overlap those measured using the micro-bulk approach but display a broader variability (Fig. 11c). They vary according to the different types of carbonates but also to their microscale textures.

Type 1 carbonates have $\delta^{13}C_{V\text{-}PDB}$ ranging from -15 to -4‰ for carbonate cores, and from -12 to -6 ‰ for veinlets. As illustrated on Fig. 11c, these values overlap the whole range of compositions measured in the carbonate veins and travertines from Oman Ophiolite.

Type 2 carbonates show a slightly more restricted range of compositions, with $\delta^{13}C_{V\text{-}PDB}$ varying from -4 to -9‰ for large calcite crystals, and from -7 to -13‰ for recrystallized microcrystals of calcite and dolomite. Finally, in contrast to Type 1 and 2 carbonates, Type 3 microcrystals $\delta^{13}C_{V\text{-}PDB}$ have values similar to those measured using the micro-bulk approach (-6 to -8‰; Fig. 11c).

$\delta^{18}O_{SMOW}$ values of Type 1 carbonates range from 31 to 26‰ in calcite cores and from 29 to 26‰ in veinlets. The low $\delta^{18}O_{SMOW}$ dolomite end-member identified in micro-bulk measurement is missing: dolomite, which represents less than 2 vol% of Type 1 carbonates, was not identified optically on analyzed thin sections and only calcite cores and veinlets were analyzed. Precipitation temperatures calculated are $T_{Ca0.0}$ = 22-39°C for calcite. These compositions and temperatures are consistent with the $\delta^{18}O_{SMOW}$ micro-bulk rock measurements of the Wadi Dima Type 1 calcites. Type 2 large calcite crystals have $\delta^{18}O_{SMOW}$ ranging from 30 to 26‰ (n = 11) and calculated precipitation temperatures $T_{Ca0.9}$ of 14-32°C. Type 2 microcrystals $\delta^{18}O_{SMOW}$ values are slightly higher than that of large calcite crystals (28-31‰, n = 8). Type 2 microcrystals comprise dolomite (MgO = 9-19 wt%) and minor Mg-calcite (MgO = 6-8 wt%), however calcite and dolomite microcrystals were too small (<20 µm) to be distinguished during analyses due to the spot size of 25 µm. Precipitation temperatures were thus calculated using the dolomite thermometer (Matthews and Katz, 1977) giving temperatures $T_{Dol0.9}$ of 15-37°C for Type 2 microcrystals. Finally, analyzed Type 3 carbonates are mainly dolomite (MgO = 18-21 wt%). They have $\delta^{18}O_{SMOW}$ from 29 to 32‰ (n = 11) and their calculated precipitation temperatures $T_{Dol0.9}$ range from 17°C to 32°C. The in situ $\delta^{18}O_{SMOW}$ values obtained in Type 2 and 3 carbonates are similar to those obtained by micro-bulk rock measurements in the same carbonate types.

5. Discussion

Carbonate precipitation in ultramafic basements is modulated by the chemical composition of the infiltrating CO_2-bearing fluids (e.g. cation and ligand concentrations, pH, alkalinity), pressure-temperature conditions, and also on the composition, mineralogy and texture of the host rocks. It is therefore strongly dependent on the geological environment. Our petro-structural study of the Wadi Dima harzburgite-hosted carbonates distinguished three carbonate types on the basis of their field relationships, microstructures and mineralogy. Type 1 carbonates are observed as a fine diffuse network, locally replacing olivine cores, penetrative into the serpentinized harzburgites. They were formed when

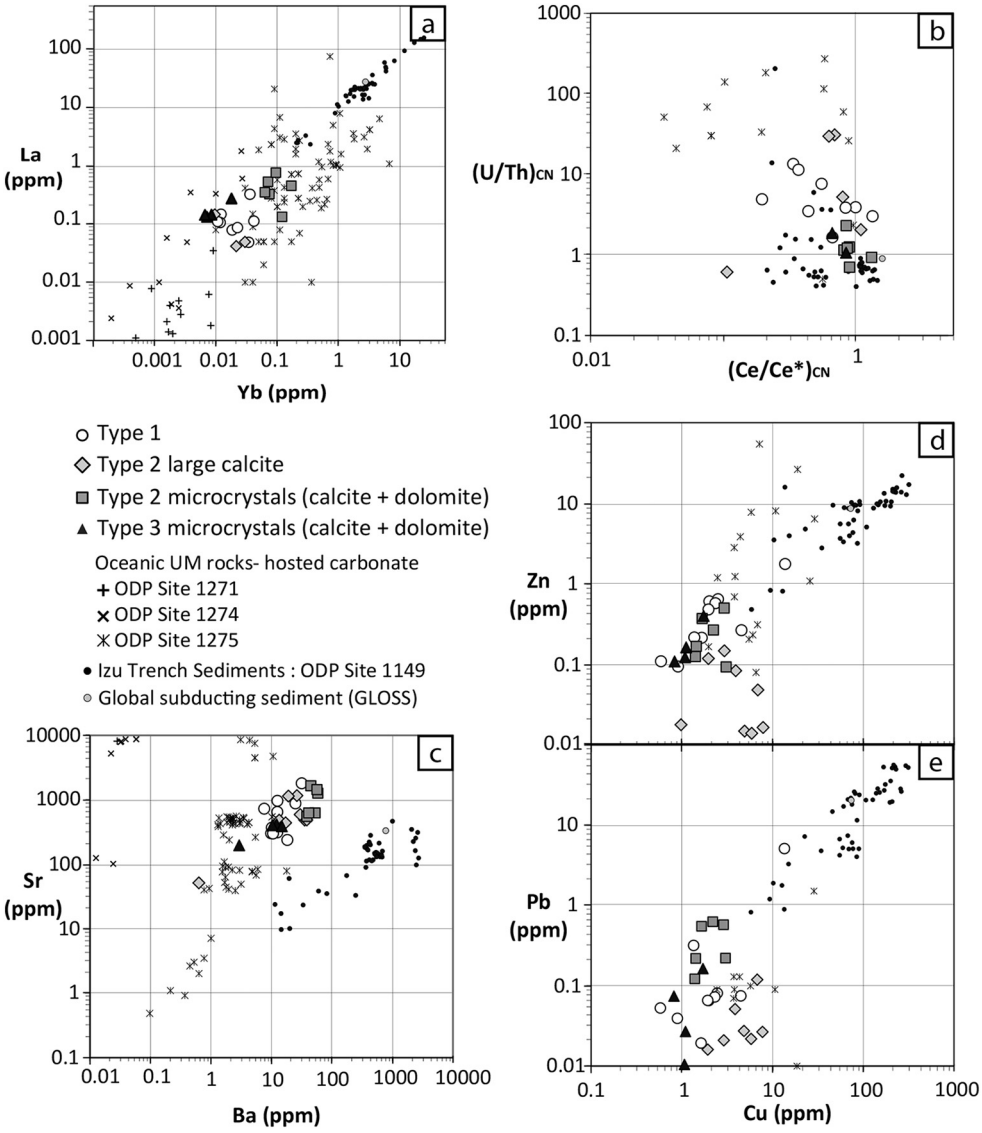

Fig. 9. (a) La (ppm) versus Yb (ppm) ; (b) U/Th versus Ce/Ce*. Correlation of high U/Th ratios and negative Ce anomalies distinguish Type 1 carbonate cores and veinlets and Type 2 large calcite crystals from Type 2 and Type 3 calcite and dolomite microcrystals; (c) Sr (ppm) versus Ba (ppm) (d) Zn (ppm) versus Cu (ppm). (e) Pb (ppm) versus Cu (ppm). The composition of sub-seafloor ultramafic-hosted hydrothermal carbonates (ODP Site 1274 serpentinized harzburgites and ODP Site 1271 and 1275 gabbro intruded impregnated ultramafic rocks; Bach et al., 2011; Schroeder et al., 2015) and of oceanic carbonate sediments conveyed toward the trench during convergence (global subducting sediment, GLOSS, composition, Plank and Langmuir, 1998; ODP Site 1149; Plank et al., 2007) is shown for comparison.

fluids pervasively penetrated the mantle basement, probably at low water-rock ratios. The composition of Type 1 carbonates was likely affected by subsequent fluid-rock interactions. In contrast to this rock-dominated system, Type 2 and 3 carbonates precipitated in fractures, some of which formed concurrently to carbonate precipitation (e.g., crack-seal textures of some Type 2 carbonates, Fig. 7). The localized flow pathways limited interactions with the mantle basement and the composition of carbonates in these fluid-dominated conditions relate to the composition of the fluid source(s) and/or interactions with carbonates already present in the fractures (evidence of recrystallization in Type 2 and 3 carbonates, Figs. 7 and 8). The physical, hydrologic and chemical processes driving the generation of these three types of carbonates are discussed in the geodynamic framework of the Oman Ophiolite formation.

5.1. Early diffuse and penetrative carbonate precipitation

Type 1 carbonate cores and veinlets display a broad range of oxygen isotopic compositions in contrast to Type 2 and 3 carbonates, with the lowest values measured in dolomite cores ($\delta^{18}O_{SMOW}$ down to 17.7‰; Fig. 11). The calculated precipitation temperatures indicate that the onset of carbonate formation occurred at hydrothermal temperatures (>100°C) locally at the expense of the serpentinized harzburgites (formation of dolomite after olivine, Figs. 4 and 5). Precipitation of dolomite then calcite continued down to temperatures overlapping those calculated for Type 2 and 3 carbonates (23-32°C). The precipitation temperatures of Type 1 carbonates overlap those of carbonates cross-cutting serpentinites in oceanic-lithosphere derived ophiolites (T°= <50-150°C, Northern Apennine, Schwarzenbach et al., 2013; T°= 38-77°C, New Caledonia, Quesnel et al., 2016; Fig. 11). Similar ranges of temperatures are also observed in hydrothermal carbonates from the oceanic ultramafic lithosphere (T°= 90-170°C; ODP Sites 1271 and 1274; Bach et al., 2011: and T°= 75-175°C; ODP Site 1275; Schroeder et al., 2015; Fig. 11); which have depleted trace element abundances similar to Type 1 carbonate cores and veinlets.

During fluid-rock interaction, the trace element composition of fluids will depend on the solubility of trace elements in the fluids and on the rock they are in contact with (e.g., via dissolution of primary

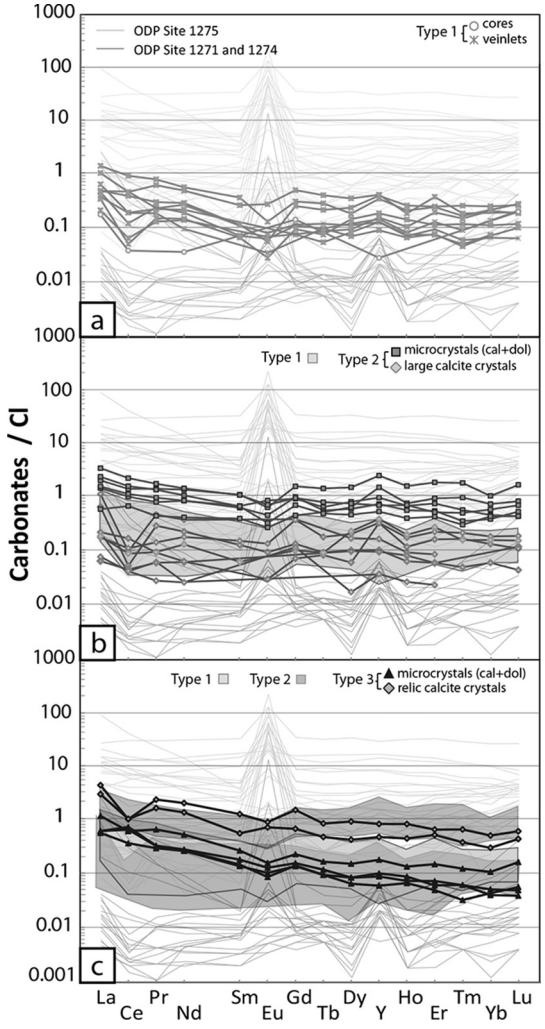

Fig. 10. Chondrite normalized Rare Earth and Yttrium (REE-Y) compositions of harzburgite-hosted carbonates (Wadi Dima area, Wadi Tayin massif). (a) Type 1 carbonate veinlets and cores; (b) Type 2 large calcite crystals and microcrystals; (c) Type 3 large calcite crystal and microcrystals. The composition of hydrothermal carbonates hosted in the oceanic ultramafic sub-seafloor (ODP Site 1274 serpentinized harzburgites and ODP Site 1271 and 1275 gabbro intruded impregnated ultramafic rocks; Bach et al., 2011; Schroeder et al., 2015) is shown for comparison.

minerals and/or (co-)precipitation of secondary minerals). The solubility of trace elements in fluids is controlled by sorption and complexation reactions, which depends numerous physico-chemical parameters (e.g., Allen and Seyfried, 2005; Bau, 1991; German et al., 1995; Migdisov et al., 2016; Pourret et al., 2008) including temperature, redox, pH and aqueous complex stability (ligands e.g., hydroxyl, chloride, fluoride, carbonate and sulfate). It is thus difficult to unravel the complexity of the changes in elemental behavior from geological records only. However, selected geochemical tracers may be used to reconstruct the conditions at which fluid-rock reactions occurred, which can be used to identify potential formation environments (i.e. in this case, oceanic or continental hydrothermal systems).

Type 1 carbonates exhibit several chemical characteristics of seawater that are commonly observed in weathered, and slightly oxidized, abyssal serpentinites, such as negative Ce and positive Y, U anomalies (e.g., Andreani et al., 2014; Boschi et al., 2006). However they do not display the strong positive Eu anomalies which characterize abyssal serpentinites (e.g., Paulick et al., 2006) and associated carbonates (Bach et al., 2011; Schroeder et al., 2015). Positive Eu anomalies in high temperature reduced serpentinization derived fluids (e.g., Douville et al., 2002; Eickmann et al., 2009) are classically attributed to (i) the alteration of plagioclase and/or (ii) the reduction of Eu(III) into Eu(II). The Eu(III)/Eu(II) redox potential decreases strongly with temperature at constant reducing conditions (Bau, 1991). The lack of gabbro in the Wadi Dima area and the low hydrothermal temperature at which Type 1 carbonates were formed likely inhibited the development of Eu anomalies. The trace element abundances and oxygen isotope compositions are consistent with Type 1 carbonates were forming from seawater-derived hydrothermal fluids, probably concurrently with low temperature serpentinization, which in turn slightly modified the composition of fluids in cooling oceanic lithosphere.

Type 1 carbonates have highly variable carbon isotopic compositions. They display the broadest range of compositions compared to the other carbonate types. Another remarkable characteristic of the carbon isotope compositions of Type 1 carbonates is the discrepancy in variability between in situ analyses, which show the broadest variability ($\delta^{13}C_{V\text{-}PDB}$ = -4.6 to -15.2‰), and micro-bulk values ($\delta^{13}C_{V\text{-}PDB\ B}$ = -6.8 to –8.4‰). This difference contrasts with results obtained for oxygen isotopes, which were consistent across both methods. Estimates of the uncertainties of carbon and oxygen isotope measurements are small relative to the observed differences between in situ and micro-bulk results. Therefore, we posit that the strong carbon isotopic variability of the in situ dataset reveals actual microscale (<100 μm) variations in the carbon isotopic compositions. These variations were partially to completely averaged by micro-bulk analyses.

The micro-bulk-rock $\delta^{13}C_{V\text{-}PDB}$ values measured in Type 1 carbonates generally overlap the range of magmatic CO_2 composition ($\delta^{13}C_{V\text{-}PDB}$ = -8 to -4‰; Pineau and Javoy, 1994; Fig. 11). These compositions are unexpected for oceanic hydrothermal carbonate veins that commonly have seawater values ($\delta^{13}C_{V\text{-}PDB}$ ~0‰). However, they are similar to the composition of abyssal serpentinites (e.g., Früh-Green et al., 2004) and to that of ophiolite serpentinites and associated carbonates (Schwarzenbach et al., 2013, 2016; Zedef et al., 2000). The range of in situ carbon isotopic compositions of Type 1 carbonates is consistent with that of the hydrogen-rich fluids sampled at low temperature ultramafic-hosted vents (e.g., Lost City Hydrothermal Field, Proskurowski et al., 2008; Lang et al., 2018). This range suggests a strong contribution of mantle derived carbon (magmatic CO_2 composition), as well as a fraction of ^{13}C depleted values ($\delta^{13}C_{V\text{-}PDB}$ < -11‰) which may indicate a contribution from a reduced organic carbon component. Organic carbon is most commonly associated with microbial activity, but studies of carbon from Lost City–type hydrothermal fluids and serpentinized oceanic basement have shown that serpentinization reactions could lead to carbon reduction reactions, and to the abiotic production of organic carbon components (e.g., reaction (R6) Fischer-Tropsch-type-reduction; Früh-Green et al., 2004; Delacour et al., 2008). This particularly light $\delta^{13}C$composition has also been observed in carbon deposits on vesicle walls and cracks in basaltic glasses (($\delta^{13}C_{V\text{-}PDB}$ = -16 ± 4‰; Pineau and Javoy, 1994). In ophiolites, depleted $\delta^{13}C$ values are generally attributed to decarboxylation of organic matter-rich sediments from the underlying accretionary complexes (Schwarzenbach et al., 2016; Zedef et al., 2000). However, the overlap in carbon isotopic composition between serpentinites and the composition of the fluids after which Type 1 carbonates formed suggests that Type 1 carbonates precipitated concurrently to serpentinization and/or from preserved reduced fluids (e.g. from fluid inclusions). Furthermore, the carbon isotopic composition of the Oman listvenites (peridotites carbonatized after reactions with subducted sediment-derived fluids) have less depleted $\delta^{13}C$ values (-3.62 to 0.99‰; Falk and Kelemen, 2015) than those measured in Type 1 carbonates. To be consistent with the other geochemical data that suggest a seawater source for cations, we posit that the Type 1 carbonate lighter carbon isotopic values result from contemporaneous carbonatization and serpentinisation reactions. This assumption implies that the carbon measured in Type 1 carbonates and the full variability of its isotopic compositions is controlled by local scale fluid-mineral reactions.

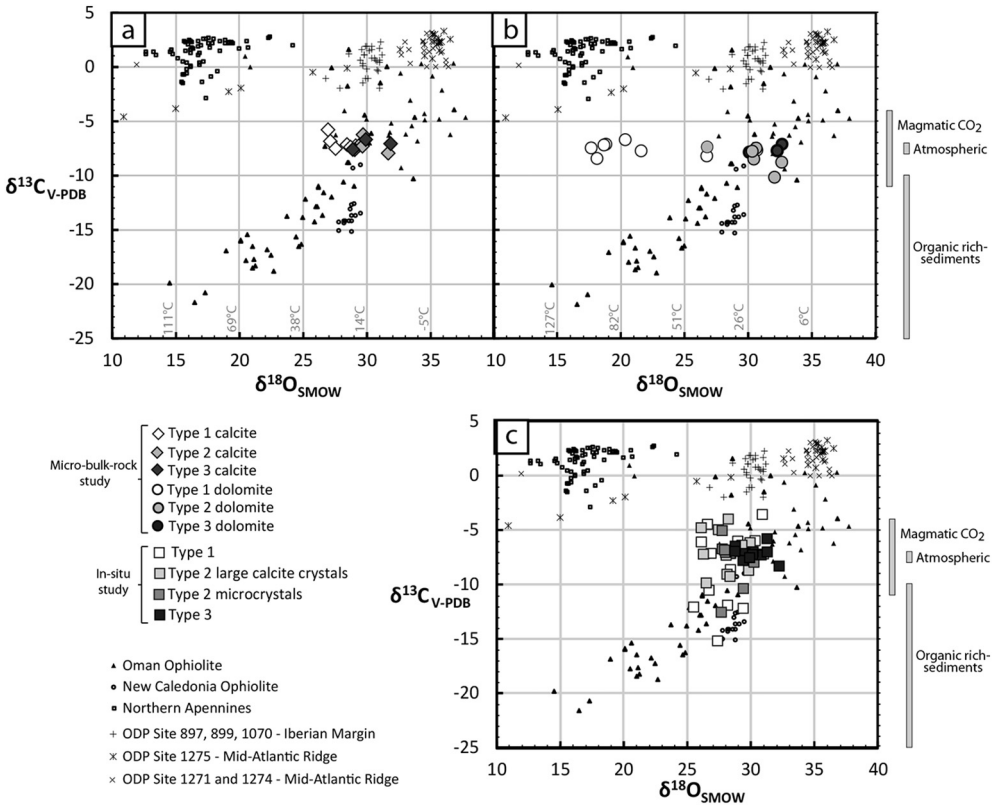

Fig. 11. Micro-bulk carbon and oxygen isotopic compositions of (a) calcite and (b) dolomite and (c) in situ carbon and oxygen isotopic compositions of the three types of harzburgite hosted carbonates. Calculated temperatures for calcite T_{CA} (Friedman and O'Neil, 1977) and dolomite T_{DOL} (Matthews and Katz, 1977) are presented. The bulk-rock carbon and oxygen isotopic compositions of carbonates veins and travertine in the Oman Ophiolite (Clark and Fontes, 1990; Kelemen et al., 2011), magnesite veins in the New Caledonia Ophiolite (Quesnel et al., 2016), sub-seafloor ultramafic-hosted hydrothermal carbonates (ODP Site 1274 serpentinized harzburgites and ODP Sites 1271 and 1275 gabbro-intruded impregnated ultramafic rocks; Bach et al., 2011; Schroeder et al., 2015) and inorganic carbon in oceanic serpentines sampled from Iberian Margin ODP Site 897, 899, 1070 in addition to Northern Apennine serpentines and ophicalcites (Schwarzenbach et al., 2013) are shown for comparison. Likely compositions of potential carbon sources including magmatic CO_2 (Früh-Green et al., 2004), atmospheric CO_2 (O'Neil and Barnes, 1971), and organic rich-sediments (Zedef et al., 2000) are presented.

Type 1 carbonates are localized in grain boundaries and along serpentine veins, indicating that the fluids from which carbonates were formed, percolated throughout the permeable serpentinized and/or serpentinizing peridotites. Peridotites and partly altered peridotites are characterized by low permeability (10^{-19}-10^{-17} m^2; Hatakeyama et al., 2017), yet the extensive serpentinization of Wadi Dima harzburgites indicates that they are efficiently infiltrated by hydrous fluids. Serpentinized peridotites are crosscut by a network of fine cracks within which serpentine and associated secondary minerals including carbonates and oxides are localized. These cracks are believed to represent the principal flow paths, facilitating the pervasive fluid infiltration into serpentinizing peridotite basements. Recent high-resolution studies of oceanic serpentinites have documented the development of a nano-porosity (<< 10μm) in association with serpentinization (Tutolo et al., 2016); this porosity, even poorly connected, could represent up to 4% of the total volume of serpentines. In parallel, reactive transport experiments of serpentinization and carbonatization into permeable peridotite analogues have demonstrated that the initial structure of the sample (distribution and structure of minerals and porous network) determined a heterogeneous distribution of flow paths and velocity, which in turn favored the development of different reaction paths at the pore scale (Andreani et al., 2009; Godard et al., 2013; Peuble et al., 2015a, 2015b). These processes resulted in a heterogeneous distribution of secondary minerals of variable composition in the percolated reacted samples in relation to pore-scale mixing and dissolution-precipitation efficiency. The infiltration of Ca-bearing CO_2-rich fluids into a dissolving olivine matrix has been demonstrated to induce precipitation of Mg-carbonates in mixing zones, and Ca-carbonates in high flow areas (Peuble et al., 2015b). We speculate that similar local variations in flow paths, mixing and reactivity account for the variability of compositions of Type 1 carbonates in Wadi Dima.

5.2. Carbonate veins, dynamic recrystallization and fluid flow

Type 2 carbonates precipitate in veins and dilatant fractures. Oxygen isotopic compositions indicate precipitation in a cooler environment (< 50°C) compared to that of Type 1 carbonates, suggesting near surface precipitation. Carbon isotopic compositions overlap in composition with Type 1 carbonates for in situ carbon isotopic values ($\delta^{13}C$ = -4.1 to -9.3‰) although they do not exhibit the same extreme range of values (in particular the very low $\delta^{13}C$). Micro-bulk $\delta^{13}C$ values are close to the isotopic composition of atmospheric CO_2 ($\delta^{13}C$ = -7 to -8‰; O'Neil and Barnes, 1971; Fig. 11). We suggest that Type 2 carbonate veins precipitated from near surface fluids having high pH, low dissolved inorganic carbon (DIC) contents and carbon isotopic composition in equilibrium with atmospheric CO_2 and likely in shallow seawater or emerged above sea level (Clark et al., 1992). In a closed system without constant input of atmospheric CO_2, the reaction can proceed to completion, and thus precipitated carbonates would exhibit the atmospheric carbon composition of -7 to -8‰.

Our microstructural study uncovered at least two generations of Type 2 veins characterizing a progressive transition in fluid flow and chemical transport conditions. The first vein generation produces large calcite crystals with trace elements compositions similar to that of Type 1 carbonates. This vein generation probably precipitated from seawater-derived fluids during the early stages of obduction, while the

ophiolite was still submerged. Large calcite crystals crystallize perpendicular to vein boundaries, likely during the opening of the veins (syntaxial texture; Bons et al., 2012). Crack-seal textures are also observed indicating fracture opening and carbonate precipitation occurred as coupled processes throughout the formation of Type 2 carbonates. The second generation of Type 2 carbonates comprises calcite and dolomite microcrystals. Microcrystals were formed at the expense of large parent calcite crystals (first generation) by dissolution – dynamic recrystallization mechanisms, implying that fluid flow was focused into Type 2 carbonate veins, which acted as a permeable medium to the out-of-equilibrium fluids. A fluid enriched in Mg (basement interaction) and in Ca (calcite dissolution) may permit simultaneous precipitation of both calcite and dolomite. In this system, the presence of Ca in the fluid does not permit precipitation of pure Mg-carbonate (magnesite $MgCO_3$ as in reaction 1), and instead calcite and dolomite microcrystals precipitate. Microcrystals are distinguished from large parent calcite crystals by their higher REE, Zn and Pb abundances indicating a change in fluid composition. A contribution from a sedimentary source characterized by higher concentrations in (bi-)carbonate and/or sulfate similar to that measured in today in Oman sedimentary aquifers (e.g., Matter et al., 2006) is possible. These components could have favored the formation of REE complexes, thus increasing their dissolved concentrations in the fluid, and thus abundances in precipitated carbonates. Micro-bulk calcite, dolomite and in situ analyses do not show significant differences in $\delta^{18}O_{SMOW}$ values. Therefore, the transition from syntaxial textures to microcrystals was not driven by temperature variations.

In contrast to Type 1 carbonates that are intimately associated with serpentinized harzburgites, Type 2 carbonates precipitate in fractures, implying efficient fluid renewal. Therefore, we suggest that the observed heterogeneities in geochemical and carbon isotopic compositions result principally from mixing in the vein network, and that the change of the fluid geochemistry from the early to late stages of Type 2 carbonates represents a change in the fluid source(s) feeding the hydrogeological system (Matter et al., 2006; Weyhenmeyer et al., 2000). Trace element enrichments and carbon isotopic compositions suggest a contribution of (possibly organic-rich) sedimentary components, suggesting that these later stages of Type 2 carbonates occurred during the transition from oceanic to obduction conditions, or even after obduction of the Oman Ophiolite (Schwarzenbach et al., 2016).

The most remarkable feature of Type 2 carbonate veins is their spatial distribution (i.e. their orientation) and their structure in relation to the initial foliation of cross-cut harzburgites. The foliation of mantle peridotites as recorded by olivine CPO indicates the direction of mantle flow in high temperature asthenospheric conditions (Nicolas, 1989). Type 2 carbonate veins form a network of three mutually perpendicular structural planes (Fig. 3). Two dominant planes are sub-vertical and directly related to olivine CPO in the hosting-harzburgite. A similar structural relationship between the primary microstructure of mantle peridotites and the distribution of serpentinization has already been reported by Dewandel et al. (2005) for the Oman Ophiolite. Boudier et al. (2005) showed that flow paths for hydrothermal fluids are localized in cracks which orientation is determined by the anisotropic crystallographic fabric of deformed mantle rocks (Boudier et al., 2009; Bouhifd et al., 1996). This micro-crack network develops due to mineral retraction during the earliest stages of mantle cooling from magmatic to hydrothermal domains. Our data suggest that the distribution of fractures and flow paths is controlled by the inherited peridotite anisotropy. This observation corroborates the dominant control of inherited peridotite anisotropy over applied stress. The initial mantle anisotropy will determine the distribution of serpentine veins; serpentine veins and wallrock will act in turn as main flow paths for carbonatization.

The development of cracks and fractures in mantle rocks during serpentinization and carbonatization is the principal mechanism facilitating their complete alteration, as these reactions are expected to efficiently clog flow paths (Kelemen et al., 2011). Fracturing is commonly ascribed to regional tectonic stress (Boudier et al., 2005), reaction-driven cracking (e.g., Jamtveit et al., 2009; Kelemen et al., 2011; Kelemen and Hirth, 2012; Macdonald and Fyfe, 1985; Plümper et al., 2012; Rudge et al., 2010; Zhu et al., 2016) and/or a combination of thermal and tectonic stresses (Rouméjon and Cannat, 2014). Stress distribution in the oceanic mantle lithosphere varies from the ridge to off-axis; in the Oman Ophiolite, the distribution of stress will have been further perturbed during the convergence and obduction (formation of the ophiolite). These changes of stress distribution are expected to favor brittle behavior of mantle rocks. Reaction-driven cracking is based on the model that the volume expansion in an elastically confined volume can cause an increase of stress and create fractures (MacDonald and Fyfe, 1985). The growth of low density secondary minerals as serpentine or carbonate compared to primary minerals (olivine, pyroxene) is thus expected to produce an increase in volume and stress-induced fractures during mass-constant serpentinization and carbonatization (Jamtveit et al., 2009; Kelemen and Hirth, 2012; Plümper et al., 2012; Rudge et al., 2010; Zhu et al., 2016).

Recent work has suggested that localization of stress at the tip of dissolution etch pits of olivine may contribute to the early formation of a pervasive microcracks network in the serpentinizing mantle (Peuble et al., 2018; Plümper et al., 2012). Etch pits are localized mainly on the (010)olivine surface/grain boundary. We speculate that this process will in turn enhance the effect of the initial mantle anisotropy on cracks and flow path distribution, in particular in relation to diffuse/penetrative fluid infiltration such as that recorded by Type 1 carbonates.

Our data suggest that this initial anisotropic CPO fabric in the peridotite controls the orientation of late brittle veins, possibly in relation to changes in larger scale tectonic conditions during cooling. Hence, it is worth noting that Type 2 carbonates are associated with serpentine selvages, suggesting either that (1) input of CO_2- bearing fluid flow was focused in already existing large serpentine veins (filled-fractures?) and/or (2) infiltration of CO_2-bearing fluids induced both serpentinization and carbonate precipitation reactions, with fluid flow initiating as localized porous flow followed by fracturing along the main flow direction. The similarities in composition between Type 1 and early Type 2 carbonates and their textural relationships across selvage serpentinites lead us to favor the second hypothesis. It implies that the transition from Type 1 carbonate mantle-dominated hydrothermalism to Type 2 vein-focused fluid-dominated carbonate systems occurred as a protracted continuous process marked by porous flow localization, followed by fracturing and a change in fluid composition.

5.3. Formation of late carbonate-vein network

Late carbonate veins (Type 3) outcrop as large, mainly sub-horizontal, veins. Their morphology in the field and textural relationship with the host rock indicates that they were formed as fractures re-activating Type 2 carbonate veins. They have oxygen isotopic compositions ($\delta^{18}O_{SMOW}$~ 28 to 32‰) consistent with carbonate precipitation at low temperatures (T°<30°C). In contrast to Type 1 and 2 carbonates, the carbon isotopic composition of Type 3 carbonates shows no significant difference between in situ and micro-bulk measurements ($\delta^{13}C_{V\text{-}PDB}$ ~ -7 to -8‰) indicating a well homogenized carbon source. They overlap in composition with the Jebel Akhdar aquifers (Matter et al., 2006; Weyhenmeyer et al., 2000), which suggests a carbonate precipitation from surface/meteoric waters, similar to Type 2 carbonates.

Type 3 carbonates are dominated by recrystallized calcite and dolomite microcrystals, interspersed with localized relics of larger parent calcite crystals. Similar to Type 2 carbonates, they display differences of trace element abundances between early large calcite crystals and late recrystallized grains indicating a change of sources during their formation. Type 3 large calcite crystals have enriched REE-Y compositions overlapping that of Type 2 carbonates, suggesting a contribution of similar sediment-derived sources for the CO_2-bearing fluids after which they were formed. Type 3 carbonates show locally high, but texturally-independent abundances of Ni and Co abundances compared to

Type 2 carbonates; these compositions are commonly associated with fluid-rock interaction. The Mg-rich compositions (inducing dolomite recrystallization) suggest that these high-pH alkaline fluids were affected by extensive interactions with the peridotite host rock, probably in relation to late low temperature serpentinization process or to weathering. Type 3 carbonates contain abundant dolomite microcrystals that indicate interaction with Mg- rich waters. The fluids sampled in Wadi Dima (Paukert et al., 2012) have high pH (up to 10), low dissolved inorganic carbon and high Mg^{2+} and low Ca^{2+}. Using PHREEQC (Parkhurst and Appelo, 1999; Database llnl.dat; id: llnl.dat 9461 2015-04-02 21:46:29Z), we calculated saturation indices of calcite and dolomite in Wadi Dima waters after interaction with a previous calcite, to model the effects of the dynamic recrystallization, at temperatures ranging from 100 to 10°C. Dolomite and calcite display high saturation indices (SI ~7-8 and ~ 4 respectively) at all temperatures suggesting conditions favorable to dolomite precipitation.

These structural, textural and chemical characteristics of Type 3 carbonates suggest that they precipitated principally from surficial/meteoric waters. The transition from Type 2 to Type 3 carbonates is marked by the reactivation of sub-horizontal Type 2 veins, in which Type 3 carbonates are focused, and occurred in relation to a change in the regional tectonic stress. We suggest that fracturing and reactivation of sub-horizontal Type 2 veins occurred during isostatic decompression caused by uplift and synchronous ophiolite erosion during the late Paleocene-Eocene. This late fracture network probably became one of the main natural hydraulic plumbing systems feeding (or being fed by) modern wadis and alkaline springs in the Oman mountains. The change of fluid source occurred after the development of the Type 3 fracture network. The Mg-rich composition of the waters flowing through the Type 3 carbonate network suggests a persistent source for Mg. The dissolution of mafic minerals from the mantle section of the Oman Ophiolite (weathering, active serpentinization) is still ongoing today.

6. Summary and conclusions

This paper presents a multiscale petro-structural and geochemical study of the carbonates of the mantle section exposed in Wadi Dima area (Oman Ophiolite). This approach allowed reconstruction of the sequence of carbonate precipitation in this area, and the context of this sequence with respect to the geodynamic evolution of the Oman ophiolite. It also highlighted the role of the initial microstructure of the mantle on the spatial distribution of late fractures and flow paths and in the development of geochemical heterogeneities at all scales during hydrothermal alteration from mid-ocean ridge to modern ophiolitic environments. Wadi Dima carbonates display variable Mg-Ca compositions overlapping the whole range of values between calcite and dolomite end-members. Three types of carbonates were identified on the basis of their structural field relationships to the host harzburgites and of their morphology.

Type 1 carbonates record the first stages of carbonate precipitation, which occur as a pervasive and diffuse process forming carbonate veinlets and cores. They form over a broad temperature range (> 100°C to 15°C) and they have depleted trace element geochemistry, as expected from precipitation from seawater-derived fluids and/or from fluids in equilibrium with refractory mantle rocks and serpentines. These first stages of carbonatization are strongly controlled by mechanical and local chemical processes, probably in relation to concurrent serpentinization. We posit that, at this early stage, the composition of fluids and therefore the efficiency of carbonate reactions is determined by pore-scale fluid-rock interactions. In this rock-dominated system, local variations in permeability and composition of the infiltrated serpentinized harzburgites likely control the composition of carbonate-forming fluids, in addition to reaction paths and reaction efficiency. We suggest that the onset of carbon-trapping reactions followed serpentinization and occurred within of cooling shallow mantle lithosphere cooling down to off-axis temperatures on the flanks of the mid-ocean ridge.

The formation of Type 2 carbonates marks the transition from this diffuse penetrative and rock-dominated hydrothermal system to a cold environment where fluid flow is focused by dilatant fractures forming veins. Carbonate geochemistry suggests precipitation from fluids sampling a breadth of different sources, including contributions of sediment-derived components. A two-stage precipitation / recrystallization process is highlighted here by (1) the precipitation of large parent calcite crystals after fluid flow in open fractures (syntaxial textures) following by (2) the fluid-assisted dynamic recrystallization of dolomite and calcite microcrystals at the expanse of the parent calcite grains (Fig. 7). Fracturing and subsequent Type 2 veins formation likely occurred during the onset of the obduction from late Cretaceous time and continued until the ophiolite emplacement.

Type 3 carbonates mark the latest stage of carbonate formation in Wadi Dima. It was initiated by a second stage of fracturing, which reactivated Type 2 veins and was probably triggered by ophiolite uplift during the Oligocene to early Miocene. The development of Type 3 carbonates veins occurred at low temperatures (T°<30°C) and also occurred as a two-stage process that starting with the precipitation of large calcite grains followed by recrystallization to finer dolomite and calcite grains. This transition was coincident with a change in fluid composition, from a composition similar to that precipitating Type 2 microcrystals to more depleted compositions. We suggest that Type 3 veins are still active today, and likely represent an essential component of the Oman Ophiolite hydrogeological systems feeding alkaline springs and wadis. The occurrence of dolomite suggests that carbonate recrystallized from Mg-rich fluids, probably originating from zones of the mantle section of the Oman Ophiolite affected by ongoing weathering or serpentinization.

A first conclusion of this study is that carbonate formation in the Oman Ophiolite is a result of successive processes associated with oceanic hydrothermal alteration to continental weathering. Our study had also two unexpected, yet outstanding, outcomes. First, it showed the strong control of the initial mantle anisotropy on the distribution and orientation of the vein network and of main flow paths from the earliest stages of serpentinization and carbonate precipitation, to late shallow post-obduction environments. Secondly, the carbon and oxygen isotopic compositions of Wadi Dima carbonates uncover significant heterogeneity reflecting local pore-scale reactive processes in poorly connected peridotites (Type 1 carbonates), and external sources in well mixed fluids in fractures (Type 2 and 3 carbonates). Further studies will be required to evaluate if these processes are observed elsewhere.

Supplementary data to this article can be found online at https://doi.org/10.1016/j.lithos.2018.08.020.

Acknowledgements

We thank R. Leprovost for his assistance for drill core sampling in the field and A. Jesus (GUTech Oman) for the drilling equipment. We would like to thank the Directorate General of Minerals in the Ministry of Commerce and Industry, Sultanate of Oman, and particularly H. Al-Azri, A. Al-Rahji and S. Al-Busaidi, for facilitating our fieldwork in Oman. This work benefited from the help of F. Barou, B. Boyer, T. Michel and O. Bruguier on analytical instruments (EBSD, EPMA, RAMAN and LA-ICPMS, respectively). We extend our thank to C. Nevado and D. Delmas for thin section preparation, B. Ildefonse and D. Mainprice for their help on MTEX software. The authors would like to thank also A. Rack & E. Boller for their assistance for the acquisition of High resolution X-ray microtomography images (ID19 beamline) and I. Williams for assistance on SHRIMP-SI and his support for our DEC proposal. We also thank two anonymous reviewers and Mr. Scambelluri (Lithos Editor) for their constructive comments that improved the manuscript. This work benefited from the AETE-ISO facilities ("Analyses des Eléments

en Trace dans l'Environnement et ISOtopes"; OREME, University of Montpellier). This study was funded by INSU CNRS Tellus project 2016 and Deep Carbon Observatory-Deep Energy community awarded by Alfred P. Sloan Foundation grant "In situ Oxygen and Carbone isotope in Oman Ophiolite basement: new insight of serpentinization, carbonatation and fluid circulation" (Sloan Subaward Number 2090 G UA721). High resolution X-ray microtomography images (ID19 beamline, ESRF, Grenoble, France) were acquired as part of ESRF Experiment ES-277. SE was supported by the People Programme (Marie Curie Actions) of the European Union's Seventh Framework ProgrammeFP7/2007-2013 under REA-Grant Agreement n608001.

References

Allen, D.E., Seyfried, W.E., 2003. Compositional controls on vent fluids from ultramafic-hosted hydrothermal systems at mid-ocean ridges: An experimental study at 400°C, 500 bars. Geochimica et Cosmochimica Acta 67:1531–1542. https://doi.org/10.1016/S0016-7037.

Allen, D.E., Seyfried, W.E., 2005. REE controls in ultramafic hosted MOR hydrothermal systems: An experimental study at elevated temperature and pressure. Geochimica et Cosmochimica Acta 69:675–683. https://doi.org/10.1016/j.gca.2004.07.016.

Alt, J.C., Garrido, C.J., Shanks, W.C., Turchyn, A., Padrón-Navarta, J.A., López Sánchez-Vizcaíno, V., Gómez Pugnaire, M.T., Marchesi, C., 2012. Recycling of water, carbon, and sulfur during subduction of serpentinites: A stable isotope study of Cerro del Almirez, Spain. Earth and Planetary Science Letters 327–328:50–60. https://doi.org/10.1016/j.epsl.2012.01.029.

Andreani, M., Mével, C., Boullier, A.-M., Escartín, J., 2007. Dynamic control on serpentine crystallization in veins: Constraints on hydration processes in oceanic peridotites. Geochemistry, Geophysics, Geosystems 8. https://doi.org/10.1029/2006GC001373.

Andreani, M., Luquot, L., Gouze, P., Godard, M., Hoisé, E., Gibert, B., 2009. Experimental study of carbon sequestration reactions controlled by the percolation of CO_2-rich brine through peridotites. Environmental Science & Technology 43:1226–1231. https://doi.org/10.1021/es8018429.

Andreani, M., Escartin, J., Delacour, A., Ildefonse, B., Godard, M., Dyment, J., Fallick, A.E., Fouquet, Y., 2014. Tectonic structure, lithology, and hydrothermal signature of the Rainbow massif (Mid-Atlantic Ridge 36°14′N). Geochemical Geophysics Geosystem 15:3543–3571. https://doi.org/10.1002/2014GC005269.

Bach, W., Rosner, M., Jöns, N., Rausch, S., Robinson, L.F., Paulick, H., Erzinger, J., 2011. Carbonate veins trace seawater circulation during exhumation and uplift of mantle rock: Results from ODP Leg 209. Earth and Planetary Science Letters 311:242–252. https://doi.org/10.1016/j.epsl.2011.09.021.

Barnes, I., O'Neil, J., Trescases, J., 1978. Present day serpentinization in New Caledonia, Oman and Yugoslavia. Geochimica et Cosmochimica Acta 42:144–145. https://doi.org/10.1016/0016-7037.

Bau, M., 1991. Rare-earth element mobility during hydrothermal and metamorphic fluid-rock interaction and the significance of the oxidation state of europium. Chemical Geology 93:219–230. https://doi.org/10.1016/0009-2541.

Beard, J.S., Frost, B.R., Fryer, P., McCaig, A., Searle, R., Ildefonse, B., Zinin, P., Sharma, S.K., 2009. Onset and progression of serpentinization and magnetite formation in olivine-rich troctolite from IODP hole U1309D. Journal of Petrology 50:387–403. https://doi.org/10.1093/petrology/egp004.

Bons, P.D., Elburg, M.A., Gomez-Rivas, E., 2012. A review of the formation of tectonic veins and their microstructures. Journal of Structural Geology 43:33–62. https://doi.org/10.1016/j.jsg.2012.07.005.

Boschi, C., Früh-Green, G.L., Delacour, A., Karson, J.A., Kelley, D.S., 2006. Mass transfer and fluid flow during detachment faulting and development of an oceanic core complex, Atlantis Massif (MAR 30°N): MASS TRANSFER AND FLUID FLOW. Geochemistry, Geophysics, Geosystems 7. https://doi.org/10.1029/2005GC001074.

Boudier, F., Coleman, R.G., 1981. Cross section through the peridotite in the Samail Ophiolite, southeastern Oman Mountains. J. Geophys. Res. 86:2573–2592. https://doi.org/10.1029/JB086iB04p02573.

Boudier, F., Nicolas, A., Mainprice, D., 2005. Does anisotropy of thermal contraction control hydrothermal circulation at the moho level below fast spreading oceanic ridges. International Geology Review 47 (1):101–112. https://doi.org/10.2747/0020-6814.47.1.101.

Boudier, F., Baronnet, A., Mainprice, D., 2009. Serpentine mineral replacements of natural olivine and their seismic implications: Oceanic lizardite versus subduction-related antigorite. Journal of Petrology 51:495–512. https://doi.org/10.1093/petrology/egp049.

Bouhifd, M.A., Andrault, D., Fiquet, G., Richet, P., 1996. Thermal expansion of forsterite up to the melting point. Geophysical Research Letters 23:1143–1146. https://doi.org/10.1029/96GL01118.

Chavagnac, V., Ceuleneer, G., Monnin, C., Lansac, B., Hoareau, G., Boulart, C., 2013a. Mineralogical assemblages forming at hyperalkaline warm springs hosted on ultramafic rocks: A case study of Oman and Ligurian ophiolites. Geochemistry, Geophysics, Geosystems 14:2474–2495. https://doi.org/10.1002/ggge.20146.

Chavagnac, V., Monnin, C., Ceuleneer, G., Boulart, C., Hoareau, G., 2013b. Characterization of hyperalkaline fluids produced by low-temperature serpentinization of mantle peridotites in the Oman and Ligurian ophiolites: Hyperalkaline Waters in Oman and Liguria. Geochemistry, Geophysics, Geosystems 14:2496–2522. https://doi.org/10.1002/ggge.20147.

Cipolli, F., Gambardella, B., Marini, L., Ottonello, G., Vetuschi Zuccolini, M., 2004. Geochemistry of high-pH waters from serpentinites of the Gruppo di Voltri (Genova, Italy) and reaction path modeling of CO2 sequestration in serpentinite aquifers. Applied Geochemistry 19:787–802. https://doi.org/10.1016/j.apgeochem.2003.10.007.

Clark, I.D., Fontes, J.-C., 1990. Paleoclimatic reconstruction in Northern Oman based on carbonates from hyperalkaline groundwaters. Quaternary Research 33:320–336. https://doi.org/10.1016/0033-5894.

Clark, I.D., Fontes, J.-C., Fritz, P., 1992. Stable isotope disequilibria in travertine from high pH waters: Laboratory investigations and field observations from Oman. Geochimica et Cosmochimica Acta 56:2041–2050. https://doi.org/10.1016/0016-7037.

Coleman, R.G., 1981. Tectonic setting for ophiolite obduction in Oman. Journal of Geophysical Research 86:2497–2508. https://doi.org/10.1029/JB086iB04p02497.

D'Alessandro, W., Yüce, G., Italiano, F., Bellomo, S., Gülbay, A.H., Yasin, D.U., Gagliano, A.L., 2018. Large compositional differences in the gases released from the Kizildag ophiolitic body (Turkey): Evidences of prevailingly abiogenic origin. Marine and Petroleum Geology, Gas Geochemistry 89:174–184. https://doi.org/10.1016/j.marpetgeo.2016.12.017.

Delacour, A., Früh-Green, G.L., Bernasconi, S.M., Schaeffer, P., Kelley, D.S., 2008. Carbon geochemistry of serpentinites in the Lost City Hydrothermal System (30°N, MAR). Geochimica et Cosmochimica Acta 72:3681–3702. https://doi.org/10.1016/j.gca.2008.04.039.

Deschamps, F., Godard, M., Guillot, S., Hattori, K., 2013. Geochemistry of subduction zone serpentinites: A review. Lithos 178:96–127. https://doi.org/10.1016/j.lithos.2013.05.019.

Dewandel, B., Lachassagne, P., Boudier, F., Al-Hattali, S., Ladouche, B., Pinault, J.-L., Al-Suleimani, Z., 2005. A conceptual hydrogeological model of ophiolite hard-rock aquifers in Oman based on a multiscale and a multidisciplinary approach. Hydrogeology Journal 13:708–726. https://doi.org/10.1007/s10040-005-0449-2.

Douville, E., Charlou, J., Oelkers, E., Bienvenu, P., Jove Colon, C., Donval, J., Fouquet, Y., Prieur, D., Appriou, P., 2002. The rainbow vent fluids (36°14′N, MAR): the influence of ultramafic rocks and phase separation on trace metal content in Mid-Atlantic Ridge hydrothermal fluids. Chemical Geology 184, 37–48.

Eickmann, B., Bach, W., Rosner, M., Peckmann, J., 2009. Geochemical constraints on the modes of carbonate precipitation in peridotites from the Logatchev Hydrothermal Vent Field and Gakkel Ridge. Chemical Geology 268:97–106. https://doi.org/10.1016/j.chemgeo.2009.08.002.

Einaudi, F., Godard, M., Pezard, P., Cochemé, J.-J., Coulon, C., Brewer, T., Harvey, P., 2003. Magmatic cycles and formation of the upper oceanic crust at spreading centers: Geochemical study of a continuous extrusive section in the Oman ophiolite. Geochemistry, Geophysics, Geosystems 4. https://doi.org/10.1029/2002GC000362.

Falk, E.S., Kelemen, P.B., 2015. Geochemistry and petrology of listvenite in the Samail ophiolite, Sultanate of Oman: Complete carbonation of peridotite during ophiolite emplacement. Geochimica et Cosmochimica Acta 160:70–90. https://doi.org/10.1016/j.gca.2015.03.014.

Falk, E.S., Guo, W., Paukert, A.N., Matter, J.M., Mervine, E.M., Kelemen, P.B., 2016. Controls on the stable isotope compositions of travertine from hyperalkaline springs in Oman: Insights from clumped isotope measurements. Geochimica et Cosmochimica Acta 192:1–28. https://doi.org/10.1016/j.gca.2016.06.026.

Friedman, I., & O'Neil, J. R. 1977. Data of Geochemistry: Compilation of Stable Isotope Fractionation Factors of Geochemical Interest (Vol. 440). US Government Printing Office.

Früh-Green, G.L., Kelley, D.S., Bernasconi, S.M., Karson, J.A., Ludwig, K.A., Butterfield, D.A., Boschi, C., Proskurowski, G., 2003. 30,000 years of hydrothermal activity at the Lost City vent field. Science 301:495–498. https://doi.org/10.1126/science.1085582.

Früh-Green, G.L., Connolly, J.A.D., Plas, A., Kelley, D.S., Grobéty, B., 2004. Serpentinization of oceanic peridotites: Implications for geochemical cycles and biological activity. In: Wilcock, W.S.D., Delong, E.F., Kelley, D.S., Baross, J.A., Cary, S.C. (Eds.), The Subseafloor Biosphere at Mid-Ocean Ridges. American Geophysical Union:pp. 119–136 https://doi.org/10.1029/144GM08.

German, C.R., Masuzawa, T., Greaves, M.J., Elderfield, H., Edmond, J.M., 1995. Dissolved rare earth elements in the Southern Ocean: Cerium oxidation and the influence of hydrography. Geochimica et Cosmochimica Acta 59, 1551–1558.

Glennie, K.W., Boeuf, M.G.A., Clarke, M.W.H., Moody-Stuart, M., Pilaar, W.F.H., Reinhardt, B.M., 1973. Late cretaceous nappes in Oman mountains and their geologic evolution. AAPG Bulletin 57, 5–27.

Godard, M., Luquot, L., Andreani, M., Gouze, P., 2013. Incipient hydration of mantle lithosphere at ridges: A reactive-percolation experiment. Earth and Planetary Science Letters 371–372:92–102. https://doi.org/10.1016/j.epsl.2013.03.052.

Griffin, W.L., Powell, W.J., Pearson, N.J., O'reilly, S.Y., 2008. GLITTER: data reduction software for laser ablation ICP-MS. Laser Ablation-ICP-MS in the earth sciences. Mineralogical Association 40, 204–207.

Hatakeyama, K., Katayama, I., Hirauchi, K., Michibayashi, K., 2017. Mantle hydration along outer-rise faults inferred from serpentinite permeability. Scientific Reports 7, 13870. https://doi.org/10.1038/s41598-017-14309-9.

Hoefs, J., 2008. Stable Isotope Geochemistry. Springer Science & Business Media.

Ickert, R.B., Hiess, J., Williams, I.S., Holden, P., Ireland, T.R., Lanc, P., Schram, N., Foster, J.J., Clement, S.W., 2008. Determining high precision, in situ, oxygen isotope ratios with a SHRIMP II: Analyses of MPI-DING silicate-glass reference materials and zircon from contrasting granites. Chemical Geology 257:114–128. https://doi.org/10.1016/j.chemgeo.2008.08.024.

Ireland, T.R., Clement, S., Compston, W., Foster, J.J., Holden, P., Jenkins, B., Lanc, P., Schram, N., Williams, I.S., 2008. Development of SHRIMP. Australian Journal of Earth Sciences 55:937–954. https://doi.org/10.1080/08120090802097427.

Jamtveit, B., Putnis, C.V., Malthe-Sørenssen, A., 2009. Reaction induced fracturing during replacement processes. Contributions to Mineralogy and Petrology 157:127–133. https://doi.org/10.1007/s00410-008-0324-y.

Janecky, D.R., Seyfried, W.E., 1986. Hydrothermal serpentinization of peridotite within the oceanic crust: Experimental investigations of mineralogy and major element chemistry. Geochimica et Cosmochimica Acta 50:1357–1378. https://doi.org/10.1016/0016-7037.

Kelemen, P.B., Hirth, G., 2012. Reaction-driven cracking during retrograde metamorphism: Olivine hydration and carbonation. Earth and Planetary Science Letters 345–348:81–89. https://doi.org/10.1016/j.epsl.2012.06.018.

Kelemen, P.B., Manning, C.E., 2015. Reevaluating carbon fluxes in subduction zones, what goes down, mostly comes up. Proceedings of the National Academy of Sciences 112: E3997–E4006. https://doi.org/10.1073/pnas.1507889112.

Kelemen, P.B., Matter, J., 2008. In situ carbonation of peridotite for CO_2 storage. Proceedings of the National Academy of Sciences 105:17295–17300. https://doi.org/10.1073/pnas.0805794105.

Kelemen, P.B., Matter, J., Streit, E.E., Rudge, J.F., Curry, W.B., Blusztajn, J., 2011. Rates and mechanisms of mineral carbonation in peridotite: Natural processes and recipes for enhanced, in situ CO_2 capture and storage. Annual Review of Earth and Planetary Sciences 39:545–576. https://doi.org/10.1146/annurev-earth-092010-152509.

Kelemen, P., Rajhi, A.A., Godard, M., Ildefonse, B., Köpke, J., MacLeod, C., Manning, C., Michibayashi, K., Nasir, S., Shock, E., Takazawa, E., Teagle, D., 2013. Scientific Drilling. Scientific Drilling. https://doi.org/10.2204/iodp.sd.15.10.2013.

Kelley, D.S., Karson, J.A., Blackman, D.K., Früh-Green, G.L., Butterfield, D.A., Lilley, M.D., Olson, E.J., Schrenk, M.O., Roe, K.K., Lebon, G.T., Rivizzigno, P., Party, Shipboard, 2001. An off-axis hydrothermal vent field near the Mid-Atlantic Ridge at 30° N. Nature 412:145–149. https://doi.org/10.1038/35084000.

Klein, F., Bach, W., Jöns, N., McCollom, T., Moskowitz, B., Berquó, T., 2009. Iron partitioning and hydrogen generation during serpentinization of abyssal peridotites from 15°N on the Mid-Atlantic Ridge. Geochimica et Cosmochimica Acta 73:6868–6893. https://doi.org/10.1016/j.gca.2009.08.021.

Lang, S.Q., Früh-Green, G.L., Bernasconi, S.M., Brazelton, W.J., Schrenk, M.O., McGonigle, J.M., 2018. Deeply-sourced formate fuels sulfate reducers but not methanogens at Lost City hydrothermal field. Scientific Reports 8. https://doi.org/10.1038/s41598-017-19002-5.

Lee, J.H., Byrne, R.H., 1992. Examination of comparative rare earth element complexation behavior using linear free-energy relationships. Geochimica et Cosmochimica Acta 56:1127–1137. https://doi.org/10.1016/0016-7037.

Macdonald, A.H., Fyfe, W.S., 1985. Rate of serpentinization in seafloor environments. Tectonophysics 116:123–135. https://doi.org/10.1016/0040-1951.

Mainprice, D., Bachmann, F., Hielscher, R., Schaeben, H., 2015. Descriptive tools for the analysis of texture projects with large datasets using MTEX: strength, symmetry and components. Geological Society, London, Special Publications 409:251–271. https://doi.org/10.1144/SP409.8.

Matter, J.M., Waber, H.N., Loew, S., Matter, A., 2006. Recharge areas and geochemical evolution of groundwater in an alluvial aquifer system in the Sultanate of Oman. Hydrogeology Journal 14:203–224. https://doi.org/10.1007/s10040-004-0425-2.

Matthews, A., Katz, A., 1977. Oxygen isotope fractionation during the dolomitization of calcium carbonate. Geochimica et Cosmochimica Acta 41:1431–1438. https://doi.org/10.1016/0016-7037.

Mervine, E.M., Humphris, S.E., Sims, K.W.W., Kelemen, P.B., Jenkins, W.J., 2014. Carbonation rates of peridotite in the Samail Ophiolite, Sultanate of Oman, constrained through 14C dating and stable isotopes. Geochimica et Cosmochimica Acta 126: 371–397. https://doi.org/10.1016/j.gca.2013.11.007.

Migdisov, A., Williams-Jones, A.E., Brugger, J., Caporuscio, F.A., 2016. Hydrothermal transport, deposition, and fractionation of the REE: Experimental data and thermodynamic calculations. Chemical Geology 439:13–42. https://doi.org/10.1016/j.chemgeo.2016.06.005.

Miller, H.M., Matter, J.M., Kelemen, P., Ellison, E.T., Conrad, M.E., Fierer, N., Ruchala, T., Tominaga, M., Templeton, A.S., 2016. Modern water/rock reactions in Oman hyperalkaline peridotite aquifers and implications for microbial habitability. Geochimica et Cosmochimica Acta 179:217–241. https://doi.org/10.1016/j.gca.2016.01.033.

Mirone, A., Brun, E., Gouillart, E., Tafforeau, P., Kieffer, J., 2014. The PyHST2 hybrid distributed code for high speed tomographic reconstruction with iterative reconstruction and a priori knowledge capabilities. Nuclear Instruments and Methods in Physics Research Section B: Beam Interactions with Materials and Atoms 324:41–48. https://doi.org/10.1016/j.nimb.2013.09.030.

Möller, P., Bau, M., 1993. Rare-earth patterns with positive cerium anomaly in alkaline waters from Lake Van. Turkey Earth and Planetary Science Letters 117:671–676. https://doi.org/10.1016/0012-821X.

Neal, C., Stanger, G., 1985. Past and present serpentinisation of ultramafic rocks; An example from the Semail Ophiolite Nappe of Northern Oman. The Chemistry of Weathering. Springer, Dordrecht:pp. 249–275 https://doi.org/10.1007/978-94-009-5333-8_15.

Nicolas, A., 1989. Structures of Ophiolites and Dynamics of Oceanic Lithosphere. 367. Kluwer Academic Publishers.

Nicolas, A., Boudier, F., Ildefonse, B., Ball, E., 2000. Accretion of Oman and United Arab Emirates ophiolite – Discussion of a new structural map. Marine Geophysical Researches 21:147–180. https://doi.org/10.1023/A:1026769727917.

O'Neil, J.R., Barnes, I., 1971. C13 and O18 compositions in some fresh-water carbonates associated with ultramafic rocks and serpentinites: western United States. Geochimica et Cosmochimica Acta 35:687–697. https://doi.org/10.1016/0016-7037.

Parkhurst, D.L., Appelo, C.A.J., 1999. User's guide to PHREEQC (Version 2): A Computer Program for Speciation, Batch-Reaction, One-Dimensional Transport, and Inverse Geochemical Calculations.

Paukert, A.N., Matter, J.M., Kelemen, P.B., Shock, E.L., Havig, J.R., 2012. Reaction path modeling of enhanced in situ CO2 mineralization for carbon sequestration in the peridotite of the Samail Ophiolite, Sultanate of Oman. Chemical Geology 330 (331): 86–100. https://doi.org/10.1016/j.chemgeo.2012.08.013.

Paulick, H., Bach, W., Godard, M., De Hoog, J.C.M., Suhr, G., Harvey, J., 2006. Geochemistry of abyssal peridotites (Mid-Atlantic Ridge, 15°20′N, ODP Leg 209): Implications for fluid/rock interaction in slow spreading environments. Chemical Geology 234: 179–210. https://doi.org/10.1016/j.chemgeo.2006.04.011.

Pearce, N.J.G., Perkins, W.T., Westgate, J.A., Gorton, M.P., Jackson, S.E., Neal, C.R., Chenery, S.P., 1997. A compilation of new and published major and trace element data for NIST SRM 610 and NIST SRM 612. Glass Reference Materials. Geostandards and Geoanalytical Research 21:115–144. https://doi.org/10.1111/j.1751-908X.1997.tb00538.x.

Peuble, S., Andreani, M., Godard, M., Gouze, P., Barou, F., Van, de M.B., Mainprice, D., REE-Ynard, B., 2015a. Carbonate mineralization in percolated olivine aggregates: Linking effects of crystallographic orientation and fluid flow. American Mineralogist 100: 474–482. https://doi.org/10.2138/am-2015-4913.

Peuble, S., Godard, M., Luquot, L., Andreani, M., Martinez, I., Gouze, P., 2015b. CO_2 geological storage in olivine rich basaltic aquifers: New insights from reactive-percolation experiments. Applied Geochemistry 52:174–190. https://doi.org/10.1016/j.apgeochem.2014.11.024.

Peuble, S., Andreani, M., Gouze, P., Pollet-Villard, M., REE-Ynard, B., Van de Moortele, B., 2018. Multi-scale characterization of the incipient carbonation of peridotite. Chemical Geology 476:150–160. https://doi.org/10.1016/j.chemgeo.2017.11.013.

Pineau, F., Javoy, M., 1994. Strong degassing at ridge crests: The behaviour of dissolved carbon and water in basalt glasses at 14°N, Mid-Atlantic Ridge. Earth and Planetary Science Letters 123:179–198. https://doi.org/10.1016/0012-821X.

Plank, T., Langmuir, C.H., 1998. The chemical composition of subducting sediment and its consequences for the crust and mantle. Chemical Geology 145:325–394. https://doi.org/10.1016/S0009-2541.

Plank, T., Kelley, K.A., Murray, R.W., Stern, L.Q., 2007. Chemical composition of sediments subducting at the Izu-Bonin trench. Geochemical Geophysical Geosystem 8, Q04I16. https://doi.org/10.1029/2006GC001444.

Plümper, O., Røyne, A., Magrasó, A., Jamtveit, B., 2012. The interface-scale mechanism of reaction-induced fracturing during serpentinization. Geology 40:1103–1106. https://doi.org/10.1130/G33390.1.

Pourret, O., Davranche, M., Gruau, G., Dia, A., 2008. New insights into cerium anomalies in organic-rich alkaline waters. Chemical Geology 251:120–127. https://doi.org/10.1016/j.chemgeo.2008.03.002.

Proskurowski, G., Lilley, M.D., Seewald, J.S., Fru h-Green, G.L., Olson, E.J., Lupton, J.E., Sylva, S.P., Kelley, D.S., 2008. Abiogenic hydrocarbon production at lost city hydrothermal field. Science 319:604–607. https://doi.org/10.1126/science.1151194.

Pucéat, E., Lécuyer, C., Sheppard, S.M.F., Dromart, G., Reboulet, S., Grandjean, P., 2003. Thermal evolution of Cretaceous Tethyan marine waters inferred from oxygen isotope composition of fish tooth enamels. Paleoceanography 18:1029. https://doi.org/10.1029/2002PA000823.

Quesnel, B., Boulvais, P., Gautier, P., Cathelineau, M., John, C.M., Dierick, M., Agrinier, P., Drouillet, M., 2016. Paired stable isotopes (O, C) and clumped isotope thermometry of magnesite and silica veins in the New Caledonia Peridotite Nappe. Geochimica et Cosmochimica Acta 183:234–249. https://doi.org/10.1016/j.gca.2016.03.021.

Rabu, D., Nehlig, P., Roger, J., 1993. Stratigraphy and structure of the Oman Mountains.

Rioux, M., Garber, J., Bauer, A., Bowring, S., Searle, M., Kelemen, P., Hacker, B., 2016. Synchronous formation of the metamorphic sole and igneous crust of the Semail ophiolite: New constraints on the tectonic evolution during ophiolite formation from high-precision U–Pb zircon geochronology. Earth and Planetary Science Letters 451:185–195. https://doi.org/10.1016/j.epsl.2016.06.051.

Rouméjon, S., Cannat, M., 2014. Serpentinization of mantle-derived peridotites at mid-ocean ridges: Mesh texture development in the context of tectonic exhumation. Geochemical Geophysical Geosystem 15:2354–2379. https://doi.org/10.1002/2013GC005148.

Rudge, J.F., Kelemen, P.B., Spiegelman, M., 2010. A simple model of reaction-induced cracking applied to serpentinization and carbonation of peridotite. Earth and Planetary Science Letters 291 (1):215–227. https://doi.org/10.1016/j.epsl.2010.01.016.

Schroeder, T., Bach, W., Jöns, N., Jöns, S., Monien, P., Klügel, A., 2015. Fluid circulation and carbonate vein precipitation in the footwall of an oceanic core complex, Ocean Drilling Program Site 175, Mid-Atlantic Ridge. Geochem. Geophys. Geosyst. 16: 3716–3732. https://doi.org/10.1002/2015GC006041.

Schwarzenbach, E.M., Früh-Green, G.L., Bernasconi, S.M., Alt, J.C., Plas, A., 2013. Serpentinization and carbon sequestration: A study of two ancient peridotite-hosted hydrothermal systems. Chemical Geology 351:115–133. https://doi.org/10.1016/j.chemgeo.2013.05.016.

Schwarzenbach, E.M., Gill, B.C., Gazel, E., Madrigal, P., 2016. Sulfur and carbon geochemistry of the Santa Elena peridotites: Comparing oceanic and continental processes during peridotite alteration. Lithos 252–253:92–108. https://doi.org/10.1016/j.lithos.2016.02.017.

Searle, M.P., Cox, J., 2002. Subduction zone metamorphism during formation and emplacement of the Semail ophiolite in the Oman Mountains. Geological Magazine 139. https://doi.org/10.1017/S0016756802006532.

Seifritz, W., 1990. CO_2 disposal by means of silicates. Nature 345:486. https://doi.org/10.1038/345486b0.

Steefel, C.I., DePaolo, D.J., Lichtner, P.C., 2005. Reactive transport modeling: An essential tool and a new research approach for the Earth sciences. Earth and Planetary Science Letters 240 (3-4):539–558. https://doi.org/10.1016/j.epsl.2005.09.017.

Tutolo, B.M., Mildner, D.F.R., Gagnon, C.V.L., Saar, M.O., Seyfried, W.E., 2016. Nanoscale constraints on porosity generation and fluid flow during serpentinization. Geology 44:103–106. https://doi.org/10.1130/G37349.1.

Verkouteren, R.M., Klinedinst, D.B., 2004. Value assignment and uncertainty estimation of selected light stable isotope reference materials. NIST Special Publication 260, 149.

Weyhenmeyer, C.E., Burns, S.J., Waber, H.N., Aeschbach-Hertig, W., Kipfer, R., Loosli, H.H., Matter, A., 2000. Cool glacial temperatures and changes in moisture source recorded in Oman groundwaters. Science 287:842–845. https://doi.org/10.1126/science.287.5454.842.

Zedef, V., Russell, M.J., Fallick, A.E., Hall, A.J., 2000. Genesis of vein stockwork and sedimentary magnesite and hydromagnesite deposits in the ultramafic Terranes of Southwestern Turkey: A stable isotope study. Economic Geology 95:429–445. https://doi.org/10.2113/gsecongeo.95.2.429.

Zhu, W., Fusseis, F., Lisabeth, H., Xing, T., Xiao, X., De Andrade, V., Karato, S., 2016. Experimental evidence of reaction-induced fracturing during olivine carbonation.: Fracturing during olivine carbonation. Geophysical Research Letters. https://doi.org/10.1002/2016GL070834.